Enantiosensitive molecular compass

Philip Caesar M. Flores[1], Stefanos Carlström[1], Serguei Patchkovskii[1], Misha Ivanov[1,2,7], Vladimiro Mujica[3], Andres F. Ordonez[1,4,5] and Olga Smirnova[1,6,7]

[1]*Max-Born-Institut, Max-Born-Str. 2A, 12489 Berlin, Germany*

[2]*Insitute of Physics, Humboldt University zu Berlin, Berlin 12489, Germany*

[3]*School of Molecular Sciences, Arizona State University, Tempe, AZ 85287-1604, USA*

[4]*Department of Physics, Imperial College London, SW7 2BW London, United Kingdom*

[5]*Department of Physics, Freie Universität Berlin, 14195 Berlin, Germany*

[6]*Technische Universität Berlin, Straße des 17. Juni 135, 10623 Berlin, Germany*

[7]*Technion - Israel Institute of Technology, Haifa, Israel*

Chirality describes the asymmetry between an object and its mirror image and manifests itself in diverse functionalities across all scales of matter - from molecules and aggregates to thin films and bulk chiral materials. A particularly intriguing example is chirality-induced spin selectivity (CISS), where chiral structures orient electron spins enantio-sensitively. Despite extensive research, the fundamental origin of spin-chirality coupling, the unexpectedly large magnitude of the CISS effect, and the possible role of electromagnetic fields in it remain unclear. Here, we address these issues by examining the simplest scenario: spin-resolved photoionization of randomly oriented chiral molecules. We uncover a universal mechanism of spin-selective chiral photodynamics, arising solely from electric-dipole interactions and previously unrecognized. This mechanism embodies a chiral molecular compass — a pho-

toinduced magnetization vector that orients the photoelectron spin. It arises in photoexcited chiral molecules even under isotropic illumination, operates even in isotropic chiral media, and enables a phenomenon central to CISS: locking of the photoelectron spin orientation to molecular geometry. It shows that chiral molecules can sustain time-odd correlations whereas achiral molecules cannot. Our findings have broad implications, from unambiguously identifying the origin of CISS effect in photoionization to harvesting correlations underlying this effect in other forms of CISS in various chiral materials.

1 Introduction

Chiral molecular interactions are a remarkable example of a geometrically robust response active in living matter, maintained in complex and noisy environments and operating at ambient conditions [1,2]. It has potential for applications, e.g., in quantum technologies [3–7], with CISS being an example of useful functionality [8]. Originally observed as enantio-sensitive electron spin polarization upon transport through chiral biomolecules [9,10], CISS now encompasses a broad range of electronic processes where molecular chirality governs spin polarization [1,8]. Beyond molecular systems, solid-state materials with chiral crystal lattices exhibit a related but more complex influence on spin: they stabilize noncollinear spin textures such as skyrmion crystals - topologically nontrivial spin configurations whose formation and control are governed by the chirality of the lattice [11,12].

Many CISS-related phenomena are induced by light, suggesting the possibility of ultrafast control over spin-sensitive chemical processes via photoexcitation or photoionization. The interplay between spin and chirality naturally suggests spin-orbit coupling (SOC) as the underlying

mechanism for spin selectivity. However, several experiments have shown that SOC alone cannot explain the observed effect [13–15]. Numerous theoretical approaches including scattering theory [16–19], tight-binding models [20–24], density functional theory [25–27], scattering off magnetic impurities [28], electron correlation models [29], electron-phonon coupling [30,31], non-adiabatic coupling [32,33], and field-theoretical treatments [34] have been proposed, yet a complete understanding remains elusive [1]. Diverse challenges for interpretation emerge due to the presence of multiple factors that potentially affect this process in experimental measurements thereby complicating its analysis, e.g., leads or substrates for molecules, and impurities, defects, or spurious fields for solids.

Here, we examine the simplest yet ubiquitous example of spin-chirality coupling: spin-resolved photoionization of randomly oriented chiral molecules. Once ambiguities related to anisotropic targets or substrates, and complex detection schemes involving leads are removed, the fundamental origins of spin-chirality coupling associated with photodynamics emerge with a striking clarity in an approach which is equally applicable to photoionization and photoexcitation of randomly oriented molecules. We find that molecular chirality induces a directional bias coupled to photoelectron spin. This intrinsic molecular compass leads to a previously unreported effect: enantio-sensitive locking of molecular orientation to photoelectron spin, which is related to the core of CISS. The molecular compass operates in fields of arbitrary polarization, including fully isotropic polarization, and can yield enantio-sensitive spin-orientation locking of up to 64%, even for spin-unpolarized initial states. It bypasses the weak magnetic-field interaction, relying solely on electric-dipole interactions between the light field and the molecule.

In closed-shell molecules, photoionization directly links the spin of the cation (hole) to its orientation, establishing an initial spin–orientation correlation that can bias spin-selective phenomena in orientation-sensitive environments (e.g. interfaces or orientation-dependent molecular reactions). Although the hole spin subsequently evolves through spin–orbit and vibronic couplings, this evolution proceeds with an opposite phase in opposite enantiomers. Thus, enantio-sensitive spin-orientation locking triggers enantio-sensitive spin densities and currents in molecular cations. We show that correlations between photoelectron spin and molecular orientations underlying this phenomenon are enabled by chirality.

2 Spin-orientation locking and its relation to CISS

To isolate the intrinsic interplay between molecular chirality and spin that underlies the CISS effect from any extrinsic orientational biases, consider a gedanken experiment: photoionization of randomly oriented chiral molecules under isotropic illumination by linearly polarized light. In such conditions, the light field introduces no preferred laboratory direction, so any observed anisotropy must arise solely from the molecular structure itself. We first discuss the general requirements for such anisotropy to exist, and then rigorously derive and quantify this effect using a synthetic chiral system.

If the cation orientation $\hat{e}$ locks to the detected photoelectron spin direction along a laboratory axis $\hat{s}^L$, then we should observe different amounts of oriented cations correlated to spin-up and spin-down photoelectrons along this axis. For this correlation to exist in randomly oriented

thermal ensembles, there must exist a unique molecular axis $\hat{\boldsymbol{S}}$ along which the propensity to generate photoelectrons with a particular spin projection is maximal. This requirement implies that the correlation tensor $G_{ij} = \langle e_i s_j \rangle$ reflects an intrinsic molecular property, where $\hat{\boldsymbol{e}}$ is a unit molecular axis (e.g. molecular bond or fragment recoil direction), and $\hat{\boldsymbol{s}}$ is the spin detection axis of the photoelectron. Both are defined in the molecular frame, and the averaging $\langle \cdot \rangle$ is performed over isotropic illumination directions. Consequently, this intrinsic tensor must have a uniaxial symmetry about $\hat{\boldsymbol{S}}$. The most general second-rank tensor consistent with this symmetry can be written as

$$G_{ij} = g_{\parallel}\, \hat{S}_i \hat{S}_j + g_{\perp}\, (\delta_{ij} - \hat{S}_i \hat{S}_j), \tag{1}$$

which represents the uniaxial decomposition into longitudinal ($g_{\parallel}$) and transverse ($g_{\perp}$) components relative to the molecular axis $\hat{\boldsymbol{S}}$. Accordingly, the tensor G_{ij} encodes both the geometrical alignment and the strength of the intrinsic spin–orientation coupling through the parameters $g_{\parallel}$ and $g_{\perp}$. The existence of spin–orientation locking requires a single dominant eigenaxis of this tensor, i.e., $|g_{\parallel}| > |g_{\perp}|$. If the transverse response were stronger ($|g_{\parallel}| < |g_{\perp}|$), then the maximal correlation with maximal spin-polarization would occur within the plane orthogonal to $\hat{\boldsymbol{S}}$, yielding no unique axis and thus no net correlation and thus no spin-orientation locking after orientational averaging.

For a spin-conditioned ensemble, the mean molecular orientation is $\langle \hat{\mathbf{e}} \rangle_{\hat{\mathbf{s}}} = \mathbf{G}\hat{\mathbf{s}}$, while for an orientation-conditioned ensemble—corresponding to an oriented molecule—the mean spin polarization given a fixed molecular orientation is $\langle \hat{\mathbf{s}} \rangle_{\hat{\mathbf{e}}} = \mathbf{G}^T \hat{\mathbf{e}}$ (see Methods). The symmetry requires that G_{ij} is a time-odd pseudotensor, so that the orientation $\langle \hat{\boldsymbol{e}} \rangle_{\hat{\boldsymbol{s}}}$ is a time-even polar observable, whereas the spin-polarization $\langle \hat{\boldsymbol{s}} \rangle_{\hat{\boldsymbol{e}}}$ is a time-odd axial one, consistent with their respective phys-

ical meanings. These symmetry properties constrain correlations to vanish in achiral molecules, $G_{ij} = 0$. Equivalently, in achiral molecules the pseudoscalars $g_\parallel = g_\perp = 0$. The intrinsic axial direction $\hat{\boldsymbol{S}}$ is a structural/electronic property of the molecule and does not, by itself, guarantee a measurable spin–orientation correlation. The correlation tensor [Eq. (1)] is nonzero only if the pseudoscalar couplings $g_\parallel$ and/or $g_\perp$ are nonzero. Thus, $G_{ij} = 0$ implies the absence of correlation even though $\hat{\boldsymbol{S}}$ may be well-defined; conversely, the observation of a correlation requires a chiral, time-odd coupling (nonzero pseudoscalar amplitude) to the intrinsic axis.

It is convenient to rescale the pseudovector $\hat{\boldsymbol{S}}$ as $\boldsymbol{\mathcal{S}} = \sqrt{|g_\parallel|}\,\hat{\boldsymbol{S}}$ such that the tensor G_{ij} can be represented in a more compact form involving two dimensionless parameters: the pseudoscalar $\kappa = \mathrm{sign}(g_\parallel)$ and the scalar $\gamma = g_\perp/g_\parallel < 1$ quantifying the relative transverse response: $G_{ij} = \kappa\left[\mathcal{S}_i\mathcal{S}_j + \gamma\left(|\mathcal{S}|^2\delta_{ij} - \mathcal{S}_i\mathcal{S}_j\right)\right]$. The pseudovector $\boldsymbol{\mathcal{S}}$ can be regarded as an *enantiosensitive molecular compass* as it encodes both the presence of chiral coupling and its directionality. This implies that photoexcitation or photoionization under isotropic illumination, without any influence from the magnetic component of light, can effectively "magnetize" an excited or photoionized molecule. Such *molecular compass* is unique to chiral molecules.

After averaging over random molecular orientations ρ the spin–conditioned orientation yields:

$$\left\langle \langle \hat{\mathbf{e}} \rangle_{\hat{\mathbf{s}}} \right\rangle_\rho = \left\langle \mathbf{G}\hat{\mathbf{s}} \right\rangle_\rho = \frac{g_\parallel}{3}\left(1 + 2\gamma\right)\hat{\boldsymbol{s}}^L. \tag{2}$$

In the laboratory frame, the corresponding detection directions are obtained by rotation R_ρ: $\hat{\mathbf{e}}^L = R_\rho\hat{\mathbf{e}}$, $\hat{\mathbf{s}}^L = R_\rho\hat{\mathbf{s}}$. Equation (2) is a manifestation of enantio-sensitive spin-orientation locking: cations correlated with photo-electrons having positive (negative) spin projection onto the detection

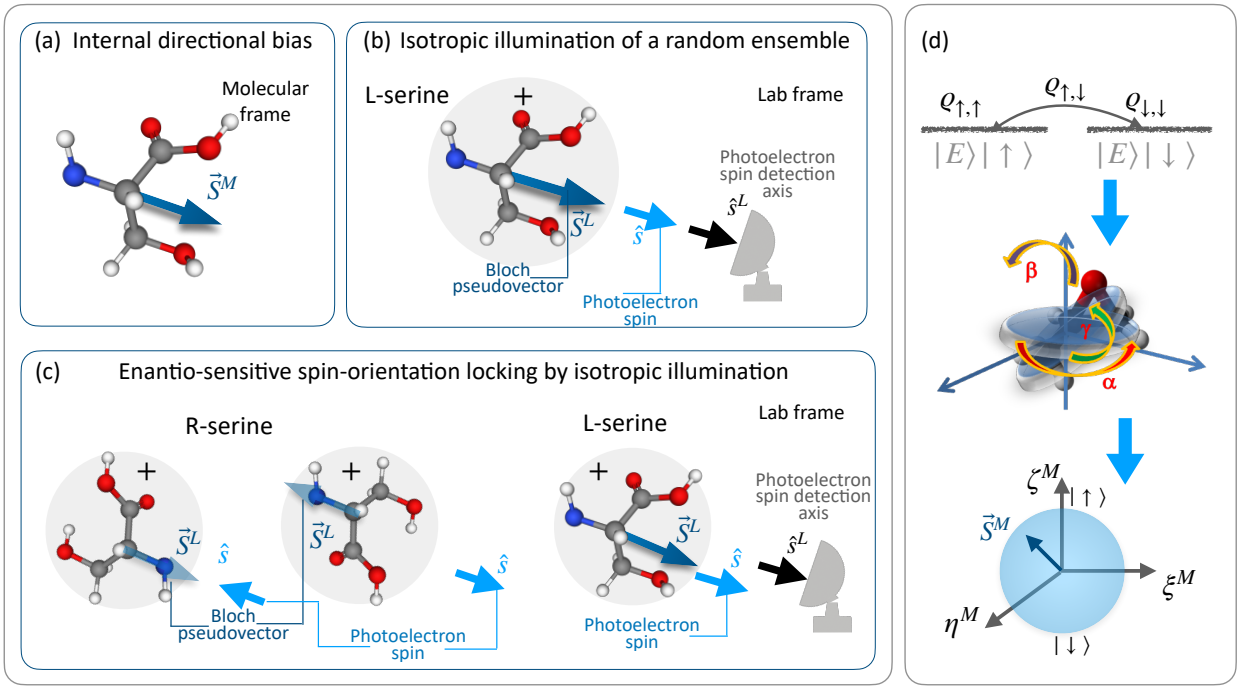

Figure 1: Spin-chirality coupling in photoionization of randomly oriented molecules under isotropic illumination is unique to chiral media. (a) The Bloch vector $\vec{\boldsymbol{S}}^M$ is "attached" to the molecule and represents the direction of molecular compass in chiral molecules . (b) After photoionization the cation cloud (grey) correlated to photoelectrons with specific spin projection on the spin detection axis $\hat{\boldsymbol{s}}^L$ possesses a net orientation such that $\vec{\boldsymbol{S}}^L$ is parallel to $\hat{\boldsymbol{s}}^L$. (c) The direction of spin to cation orientation locking is enantio-sensitive: the photoelectron spin is parallel (antiparallel) to $\vec{\boldsymbol{S}}^L$ for right (left) molecules. (d) The density matrix ρ of a degenerate two-level system corresponding to spin-up $|\uparrow\rangle$ and spin-down $|\downarrow\rangle$ states of the photoelectron with energy $E = \frac{k^2}{2}$ can be averaged over molecular orientations to yield reduced density matrix ϱ. The Bloch vector $\vec{\boldsymbol{S}}^M$ is defined on the Bloch sphere in the molecular frame $\{\hat{\boldsymbol{\xi}}^M, \hat{\boldsymbol{\eta}}^M, \hat{\boldsymbol{\zeta}}^M\}$, and is proportional to the expectation value of the spin operator for a state with density matrix ϱ.

axis $\hat{\boldsymbol{s}}^L$ are oriented with $\hat{\boldsymbol{S}}^L$ parallel (antiparallel) to $\hat{\boldsymbol{s}}^L$. This phenomenon, unique to chiral media, ensures opposite orientations for cations of opposite handedness linked to the same photoelectron spin, and vice versa (see Fig.1). However, this phenomenon also has an additional manifestation uncovering the nature of CISS in photoionization.

Indeed, consider an orientation-conditioned measurement corresponding to a fixed molecule, i.e., the laboratory frame coincides with the molecular frame. The same structure of the correlation tensor Eq. (1) leads to the second manifestation of spin-orientation locking – the net enantio-sensitive spin-polarization which depends on the molecular orientation $\hat{\boldsymbol{e}}^L$ with respect to molecular axis $\hat{\boldsymbol{S}}^L$ and quadratically encodes $\boldsymbol{\mathcal{S}}^L$ emphasizing its correlative origin:

$$\langle \hat{\boldsymbol{s}} \rangle_{\hat{\boldsymbol{e}}} = \mathbf{G}^T \hat{\mathbf{e}} = \kappa \left\{ (\hat{\boldsymbol{e}} \cdot \boldsymbol{\mathcal{S}})\, \boldsymbol{\mathcal{S}} + \gamma \left[|\boldsymbol{\mathcal{S}}|^2 \hat{\boldsymbol{e}} - (\hat{\boldsymbol{e}} \cdot \boldsymbol{\mathcal{S}})\, \boldsymbol{\mathcal{S}} \right] \right\}. \tag{3}$$

Under parity inversion, the laboratory frame and the axis $\hat{\boldsymbol{e}}$ are kept fixed, $\boldsymbol{\mathcal{S}}$ is parity even and remains intact, while the molecular pseudoscalar $g_{\parallel}$ changes sign $\kappa \to -\kappa$. Applying these transformations to Eq. (3) gives

$$\langle \hat{\boldsymbol{s}} \rangle_{\hat{\boldsymbol{e}}}^{\text{right}} = - \langle \hat{\boldsymbol{s}} \rangle_{\hat{\boldsymbol{e}}}^{\text{left}}. \tag{4}$$

Hence, spin polarization observed for a fixed molecular orientation reverses sign between opposite enantiomers: the effect is enantio-sensitive because it is proportional to the pseudoscalar coupling $g_{\parallel}$ while the molecular axis $\hat{\boldsymbol{S}}$ itself is parity-even. Defining the angle θ between the molecular orientation axis $\hat{\boldsymbol{e}}$ and the molecular axis $\hat{\boldsymbol{S}}$, the direction and magnitude of the spin polarization

in an oriented molecule are

$$\langle \hat{\boldsymbol{s}} \rangle_{\hat{\boldsymbol{e}}} = g_{\parallel} \Big[\cos\theta \, \hat{\boldsymbol{S}} + \gamma \, \sin\theta \, \hat{\boldsymbol{e}}_{\perp} \Big], \qquad |\langle \hat{\boldsymbol{s}} \rangle_{\hat{\boldsymbol{e}}}| = g_{\parallel} \sqrt{\gamma^2 + (1-\gamma^2)\cos^2\theta}. \tag{5}$$

Since we have established that $|\gamma| < 1$, the direction of maximal spin polarization coincides with $\hat{\boldsymbol{S}}$. Its magnitude is determined by $g_{\parallel}$, and its sign by the relative orientation of $\hat{\boldsymbol{S}}$ and $\hat{\boldsymbol{e}}$:

$$\langle \hat{\boldsymbol{s}} \rangle_{\hat{\boldsymbol{e}}}^{\max} = g_{\parallel} \, \mathrm{sign}(\cos\theta) \, \hat{\boldsymbol{S}}. \tag{6}$$

The angle $\theta = 0$ or π corresponds, respectively, to the two possible handednesses of the experimental frame.

3 Quantifying spin-orientation locking

Having established the general conditions for spin-orientation locking in photoionization and its connection to CISS, we now quantify the former effect. Mathematically, the direction of molecular axis $\hat{\boldsymbol{S}}$ is defined by a Bloch pseudovector $\vec{\boldsymbol{S}}$ describing spin orientation in the degenerate two-level system formed by spin-up and spin-down continuum states populated by photoionization. Indeed, let us introduce a reduced density matrix $\tilde{\varrho}^M$ of such a two-level system associated with a photoelectron of a given energy. This matrix

$$\tilde{\varrho}^M_{\mu_1,\mu_2} = \sum_I \int d\Theta_k^M \left(\vec{\boldsymbol{D}}^{M*}_{I,\vec{\boldsymbol{k}}^M,\mu_1} \cdot \vec{\boldsymbol{D}}^{M}_{I,\vec{\boldsymbol{k}}^M,\mu_2} \right) \tag{7}$$

naturally arises in one-photon ionization. Here, $\vec{\boldsymbol{D}}^{M}_{I,\vec{\boldsymbol{k}}^M,\mu}$ is the molecular-frame transition dipole (see Methods), I labels the final state of the ion, $\mu = \pm\frac{1}{2}$ labels the spin projections onto the molecular z-axis $\hat{\boldsymbol{\zeta}}^M$, $\vec{\boldsymbol{k}}^M$ is the final photoelectron momentum in the molecular frame, and $\int d\Theta_k^M$

denotes averaging over all directions of $\vec{\boldsymbol{k}}^M$. The reduced density matrix Eq. (7) emerges after averaging over random molecular orientations (see Methods). Since Fermi's Golden Rule ties the transition rate to the transition dipole moment, Eq. (7) serves as the analogue of a Liouville–von Neumann density matrix with light–molecule orientation averaged out.

The geometric nature of Eq. (7) is revealed by expressing it as:

$$\frac{\tilde{\varrho}^M}{\mathrm{Tr}[\tilde{\varrho}^M]} = \frac{1}{2}\left(\mathbb{I} + \vec{\boldsymbol{S}}^M \cdot \hat{\boldsymbol{\sigma}}^M\right), \tag{8}$$

where $\hat{\boldsymbol{\sigma}}$ is the vector of the Pauli spin matrices, $\mathrm{Tr}[\tilde{\varrho}^M] \equiv S_0$ is the total ionization rate, $\frac{\tilde{\varrho}^M}{\mathrm{Tr}[\tilde{\varrho}^M]}$ is the normalized reduced density matrix and $\vec{\boldsymbol{S}}^M$ is the Bloch vector controlling enantio-sensitive spin-orientation locking,

$$\vec{\boldsymbol{S}}^M = \frac{1}{S_0}\mathrm{Tr}\left(\tilde{\varrho}^M \hat{\boldsymbol{\sigma}}^M\right). \tag{9}$$

Both $\tilde{\varrho}^M$ and $\vec{\boldsymbol{S}}^M$ only depend on the photoionization (or photoexcitation) dipoles and encode the properties of molecular states.

Even in the case of isotropic illumination in chiral molecules, the Bloch vector works as a molecular compass that locks the orientation of the molecular structure to the photoelectron spin:

$$\left\langle \left\langle \hat{\boldsymbol{e}}^L \right\rangle_{\hat{\boldsymbol{s}}^L} \right\rangle_{\rho}^{\mathrm{iso}} \equiv \frac{\int d\Theta_k^M \int d\Theta_p \int d\rho W^M(\hat{\boldsymbol{k}}^M, \hat{\boldsymbol{s}}^M, \rho)\vec{\boldsymbol{e}}^L}{\int d\Theta_s^L \int d\Theta_k^M \int d\Theta_p \int d\rho W^M(\hat{\boldsymbol{k}}^M, \hat{\boldsymbol{s}}^M, \rho)} = \frac{\nu}{3}|\vec{\boldsymbol{S}}^M|\hat{\boldsymbol{s}}^L \tag{10}$$

where $\nu = \pm 1$ for opposite enantiomers (see Methods). Equation (10) defines the expectation value of the molecular vector $\vec{\boldsymbol{e}}^M$ in the photoionized ensemble of randomly oriented molecules. Here, $W^M(\hat{\mathbf{k}}^M, \hat{\mathbf{s}}^M, \rho)$ is the momentum- and spin-resolved ionization rate, while $\int d\rho$, and $\int d\Theta_p$ denotes averaging over molecular, and light field orientations, respectively. Last, $\int d\Theta_k^M$ and

$\int d\Theta_s^L$ describe averaging over directions of photoelectron momenta and spin directions, respectively. It shows that that correlations between an orientation-averaged value $\langle \vec{\boldsymbol{e}}^L \rangle$ of a molecular vector $\vec{\boldsymbol{e}}^M$ and the photo-electron spin orientation measured along the laboratory $\hat{\boldsymbol{s}}^L$ survives averaging over random orientations of the chiral molecule ($\int d\rho$) and the directions of the photoelectron momenta ($\int d\Theta_k^M$). Moreover, we can establish the lower bound on the pseudoscalar $g_{\parallel}$ characterising CISS $|g_{\parallel}| = \frac{|\vec{\boldsymbol{S}}^M|}{1+2\gamma} \geq |\vec{\boldsymbol{S}}^M|$, where $|\gamma| \leq 1$.

Although the Bloch pseudovector can exist in achiral molecules, parity symmetry forbids any spin–orientation locking. In an isotropically illuminated, randomly oriented ensemble such as, e.g., HCl, mirror reflection leaves both the molecular distribution and the light field unchanged. The laboratory spin-detection axis $\hat{\mathrm{s}}^L$, being a pseudovector, also remains invariant under reflection. If a correlation between spin and molecular orientation were present—for instance, H–Cl cations preferentially associated with spin-up electrons—the mirrored configuration would produce the opposite cation orientation (Cl–H) for the same spin direction. Because the two mirror-related outcomes are equally probable, their contributions cancel in the ensemble average, and no net spin–orientation correlation can survive in achiral molecules.

To quantify spin-chirality coupling in photoionization, we construct spin-resolved chiral electronic states in an Ar atom, rigorously incorporating electronic chirality and spin-orbit coupling. Inspired by analogous chiral hydrogenic states [35], these states combine excited-state orbitals:

$$|\psi^{\pm}_{m,\mu}\rangle = \frac{1}{\sqrt{2}} \left(|4p_m, \mu\rangle \pm |4d_m, \mu\rangle \right). \tag{11}$$

To generalize Eq. (11) for a multielectron system such as argon (see Methods), we employ an

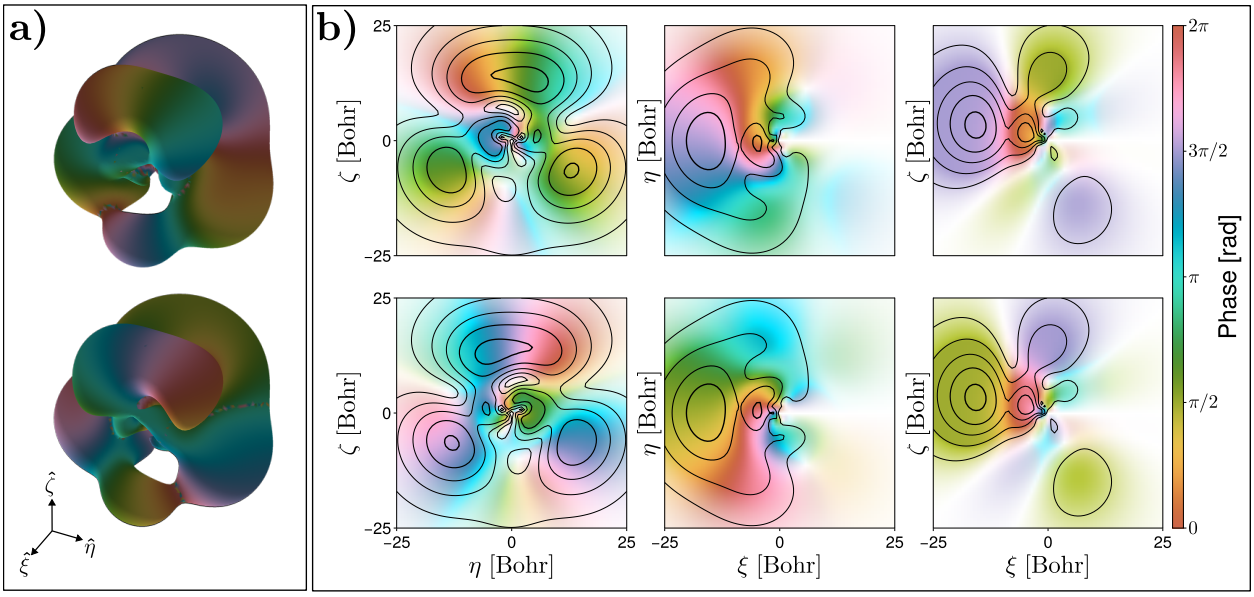

Figure 2: Comparison of the (a) isosurface and (b) contour plots of the chiral electronic states $|\psi^{+}_{-1,\frac{1}{2}}\rangle$ and $|\psi^{-}_{-1,\frac{1}{2}}\rangle$ shown in the top and bottom row (in the molecular frame), respectively, and colored according to its phase. The molecular $\{x, y, z\}$ axes are labeled as $\{\xi, \eta, \zeta\}$, respectively. The isosurface is set at $|\psi^{\pm}_{-1,\frac{1}{2}}| = 3.2 \times 10^{-3}\text{Bohr}^{3/2}$. The contour plots are cuts on the $\xi = 0$, $\zeta = 0$, and $\eta = 0$ planes. Thicker contour lines and darker shading correspond to higher values of the density. It can be seen that the probability density of the states $|\psi^{\pm}_{-1,\frac{1}{2}}\rangle$ are mirror images of each other.

optimization approach detailed in Appendix A. Unlike hydrogen, the multielectron core potential in argon breaks inversion symmetry, lowering the symmetry of the resulting states (Fig.2). Consequently, synthetic chirality in argon is stabilized by electron correlations making this system ideal for exploring spin-chirality coupling computationally within a fully consistent approach.

Figure 3 shows the degree of spin-orientation locking for different chiral states in our syn-

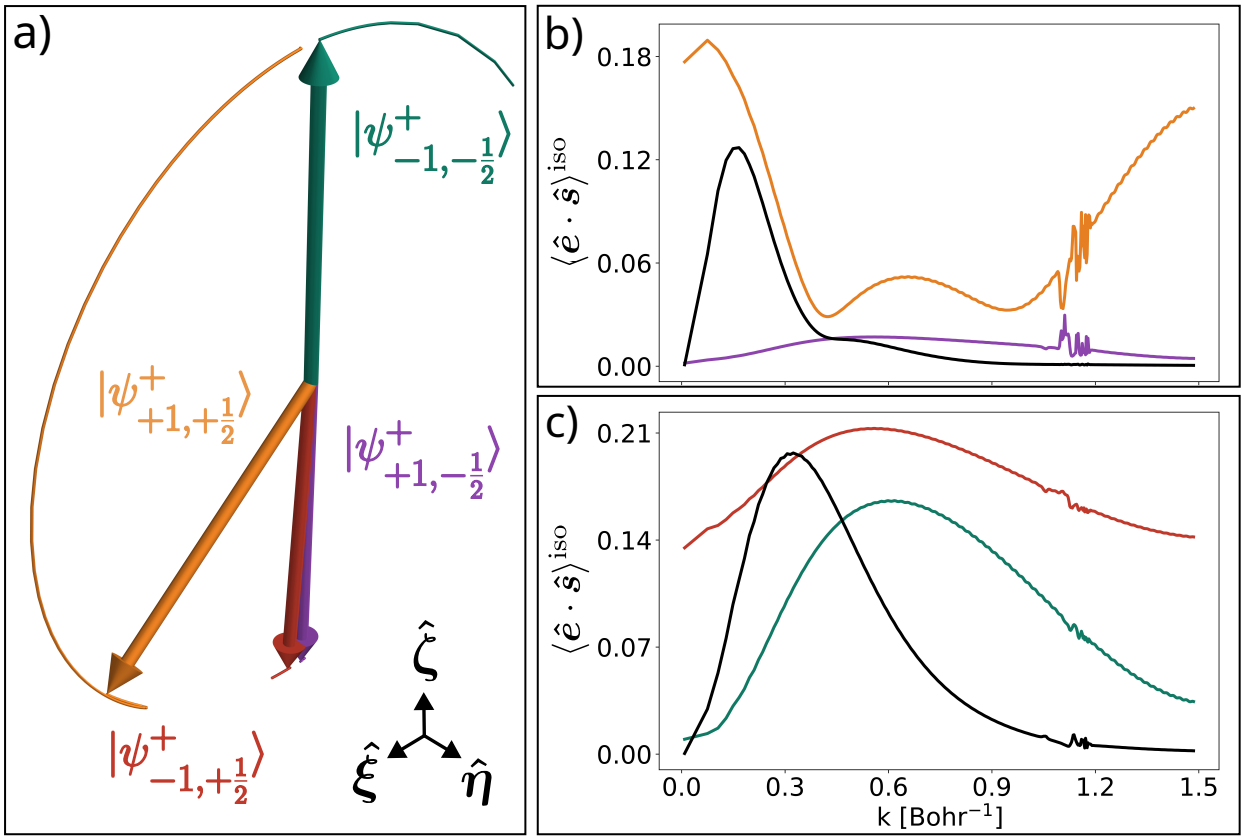

Figure 3: Enantio-sensitive spin-orientation locking under isotropic illumination of randomly oriented electronic states. (a) The Bloch pseudovector $\vec{S}^M$ (internal directional bias) in the molecular frame for the chiral argon states. $\vec{S}^M$ changes its direction in space as a function of the photoelectron momentum k. Trajectories traced by this vector are shown for $0 < k < 0.8$ Bohr^{-1}. (b) Degree of orientation for chiral states with $m = 1$, $\mu = \pm\frac{1}{2}$ (violet and orange correspondingly), and averaged over spin orientation in initial state (black). (c) Degree of orientation for chiral states with $m = -1$, $\mu = \pm\frac{1}{2}$ (red and green correspondingly) and averaged (black). The rapidly oscillating behavior at higher values of k are due to the Fano resonances, leading up to the ionization threshold for the 3s electrons [36,37].

thetic chiral system under random illumination as a function of the photoelectron momentum $k = \sqrt{2E}$. Black curves in Fig.3 (b,c) show results for photoionization from initially spin-unpolarised states, corresponding to an incoherent superposition of the chiral states with $m = 1$ and $m_s = \pm 1/2$ in Fig.3 (b) and $m = -1$ and $m_s = \pm 1/2$ in Fig.3 (c). We see strong spin-orientation locking even in such a small chiral system, with $\langle \hat{\boldsymbol{e}}^L \cdot \hat{\boldsymbol{s}}^L \rangle = \langle \cos\beta \rangle \simeq 0.13$ corresponding to about 60% of the ionized molecules oriented such that $\hat{\boldsymbol{e}}^L$ has positive projection onto $\hat{\boldsymbol{s}}^L$ for $m = 1$ initial states and $\langle \hat{\boldsymbol{e}}^L \cdot \hat{\boldsymbol{s}}^L \rangle \simeq 0.19$ corresponding to about 64% of the ionized molecules oriented such that $\hat{\boldsymbol{e}}^L$ has positive projection onto $\hat{\boldsymbol{s}}^L$ for $m = -1$ (see Methods).

The Bloch vectors for $m = 1, m_s = \pm 1/2$ are almost orthogonal to each other (see orange and violet arrows in Fig.3 (a)), while for the state $m = +1, m_s = 1/2$ the Bloch vector is orthogonal to the chosen spin quantization axis $\hat{\boldsymbol{\zeta}}^M$. The latter signifies strong contribution of coherences to the longitudinal spin-orientation locking arising during photoionization. The role of coherences in longitudinal spin polarization has not been identified before, because the latter is usually identified as the z-component of the spin expectation value in the final state, which only reflects the difference in populations of the spin-up and spin-down final states at the detector. Figure 3 also demonstrates that the direction of the Bloch vector changes as a function of the photoelectron energy.

An additional directional bias introduced by the laser field may enhance the enantio-sensitive spin-orientation locking. The well-defined direction of light polarization (circular or linear) in-

duces an additional directional bias quantified by the vector

$$\vec{\boldsymbol{S}'}^{M} = \frac{1}{S_0}\mathrm{Re}\left[\sum_{I,\mu_1^M,\mu_2^M}\int d\Theta_k^M \left(\vec{\boldsymbol{D}}^{M*}_{I,\vec{\boldsymbol{k}}^M,\mu_1^M}\cdot\hat{\boldsymbol{\sigma}}^{M}_{\mu_2^M,\mu_1^M}\right)\vec{\boldsymbol{D}}^{M}_{I,\vec{\boldsymbol{k}}^M,\mu_2^M}\right] \tag{12}$$

and also leads to two possible detection geometries in which the photoelectron spin can be detected either orthogonal ($\hat{\boldsymbol{s}}^L \perp \hat{\boldsymbol{\epsilon}}^L$) or collinear ($\hat{\boldsymbol{s}}^L \parallel \hat{\boldsymbol{\epsilon}}^L$) to the light field polarization vector $\hat{\boldsymbol{\epsilon}}^L$. In the case of linearly polarised field with orthogonal detection geometry, enantio-sensitive spin orientation locking reaches extremely high values up to 73% ($\langle\hat{\boldsymbol{e}}^L\cdot\hat{\boldsymbol{s}}^L\rangle = 0.3$ at $k = 0.6$ a.u., red curve) and 68 % ($\langle\hat{\boldsymbol{e}}^L\cdot\hat{\boldsymbol{s}}^L\rangle = 0.24$ at $k = 0.31$ a.u., black curve) , see Fig. 4(a), for spin unpolarised initial state both exceeding those for isotropic illumination, see Fig. 3(c). In this case the axis of molecular orientation is $2\vec{\boldsymbol{S}}^M + \vec{\boldsymbol{S}'}^M$ and the probability to orient molecular cations is:

$$\left\langle\langle\hat{\boldsymbol{e}}^L\rangle_{\hat{\boldsymbol{s}}^L\perp\hat{\boldsymbol{\epsilon}}^L}\right\rangle_\rho = \frac{\nu}{5}|2\vec{\boldsymbol{S}}^M + \vec{\boldsymbol{S}'}^M|\hat{\boldsymbol{s}}^L, \tag{13}$$

where $\hat{\boldsymbol{e}}^M$ is a unit polar vector along $2\vec{\boldsymbol{S}}^M + \vec{\boldsymbol{S}'}^M$ and $\hat{\boldsymbol{e}}^L$ is its ensemble averaged value. This indicates that partial alignment by photon absorption encapsulated in $\vec{\boldsymbol{S}'}^M$ indeed enhances the effect. However, collinear detection geometry results in an overall low signal, Fig. 4(b), because in this case $\vec{\boldsymbol{S}}^M$ and $2\vec{\boldsymbol{S}'}^M$ partially compensate each other:

$$\left\langle\langle\hat{\boldsymbol{e}}^L\rangle_{\hat{\boldsymbol{s}}^L\parallel\hat{\boldsymbol{\epsilon}}^L}\right\rangle_\rho = \frac{\nu}{5}|\vec{\boldsymbol{S}}^M - 2\vec{\boldsymbol{S}'}^M|\hat{\boldsymbol{s}}^L, \tag{14}$$

where $\hat{\boldsymbol{e}}^M$ is along the axis of molecular orientation $\hat{\boldsymbol{e}}^M \parallel \vec{\boldsymbol{S}}^M - 2\vec{\boldsymbol{S}'}^M$.

4 Conclusions and Outlook

Quantum correlations between the photoelectron spin and the molecular skeleton orientation are unique to chiral molecules. Importantly, they survive averaging over random molecular orienta-

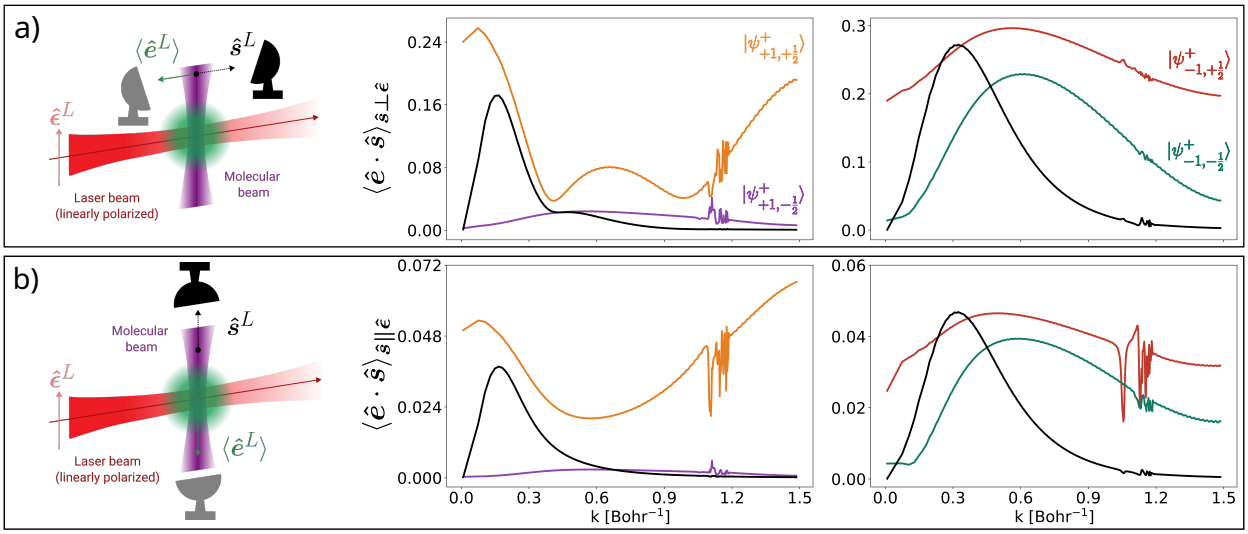

Figure 4: Enantio-sensitive spin-orientation locking resulting from illumination of randomly oriented electronic states by linearly polarised fields in (a) orthogonal detection geometry $\hat{\boldsymbol{s}}^L \perp \hat{\boldsymbol{\epsilon}}^L$ [Eq. (13)] and (b) collinear detection geometry $\hat{\boldsymbol{s}}^L \parallel \hat{\boldsymbol{\epsilon}}^L$ [Eq. (14)]. For both panels, $m = 1$, $\mu = \pm\frac{1}{2}$ (violet and orange correspondingly), $m = -1$, $\mu = \pm\frac{1}{2}$ (red and green correspondingly) and black corresponds to spin unpolarised initial state.

tions, with the coherence between the spin-up and spin-down final components of the photoelectron recorded in the Bloch pseudovector resulting from the reduced density matrix. These correlations underlie the main microscopic mechanism of chirality induced spin selectivity. We identify the photoionization Bloch vector as a chiral molecular compass mediating spin-chirality coupling and offering significant control over the orientation of enantiomers in space. Conversely, the chiral molecular compass also gives rise to enantio-sensitive spin dynamics in photoexcited oriented molecules. Our approach highlights that both the direction and magnitude of the chiral molecular compass depend sensitively on photon energy, leading to either strong or weak spin polarization

within the same chiral medium. We expect that the enantio-sensitive molecular compass is also relevant for understanding electron spin polarization in scattering from gas-phase chiral molecules [38,39] - the phenomenon that predated the formulation of the CISS effect. The enantio-sensitive molecular compass may represent a possible mechanism contributing to the long-standing puzzle of avian orientation.

Methods

The nature and the symmetry of the correlation tensor

To understand the microscopic origin of the spin–orientation correlation tensor, consider an entangled wavefunction of orientational and spin degrees of freedom,

$$|\Psi\rangle = \int d\rho c_\rho \, |\mathbf{e}_\rho\rangle \, |\mathbf{s}_\rho\rangle, \tag{15}$$

with $\varrho = |\Psi\rangle\langle\Psi|$ or, for a mixed state, the density matrix

$$\varrho = \int d\rho |c_\rho|^2 \, |\mathbf{e}_\rho\rangle \, \langle\mathbf{e}_\rho| \otimes |\mathbf{s}_\rho\rangle \, \langle\mathbf{s}_\rho| \, , \tag{16}$$

where $|\mathbf{e}_\rho\rangle$ and $|\mathbf{s}_\rho\rangle$ denote the molecular orientation and spin states in each elementary configuration ρ. The joint quantum statistics of these two observables are fully encoded in the *cross-correlation tensor*

$$G_{ij} \;=\; \langle e_i s_j \rangle \;=\; \mathrm{Tr}\Big[\varrho \, (\hat{E}_i \otimes \hat{\sigma}_j)\Big] \, , \tag{17}$$

where e_i and s_j represent orientation and spin detection axis and $\hat{E}_i$, $\hat{\sigma}_j$ are the corresponding operators acting in the orientation and spin subspaces, respectively. We use the dimensionless

Pauli matrices $\boldsymbol{\sigma} = (\sigma_x, \sigma_y, \sigma_z)$ to represent the spin direction operator, related to the physical spin operator by $\hat{\mathbf{S}} = \frac{1}{2}\boldsymbol{\sigma}$. This choice ensures that both spin-conditioned and orientation-conditioned averages are governed by the same tensor G_{ij} without additional scaling factors. The tensor G_{ij} encapsulates the full set of quantum-mechanical correlations between spin and orientation and is the same object that governs both conditional averages discussed below. Formally, it encodes how the detected orientation axis $\hat{\boldsymbol{e}}$ (time-even, polar) depends on the detection spin axis $\hat{\boldsymbol{s}}$ (time-odd, axial) and vise versa.

Let us first consider the orientation-conditioned expectation value of the spin, which can be written as

$$\langle \sigma_j \rangle_{\hat{\mathbf{e}}} = \frac{\mathrm{Tr}\{\varrho\,[F(\hat{\mathbf{e}}) \otimes \hat{\sigma}_j]\}}{\mathrm{Tr}\{\varrho\,[F(\hat{\mathbf{e}}) \otimes I]\}}. \tag{18}$$

Here, ϱ is the joint density operator of the molecular orientation and spin subsystems, while $F(\hat{\mathbf{e}})$ is a positive-operator-valued measure (POVM) element acting in the molecular-orientation subspace. It represents the measurement of the molecular axis direction $\hat{\mathbf{e}}$ and corresponds to a finite solid-angle window around that direction on the sphere. It satisfies $F(\hat{\mathbf{e}}) \geq 0$ and the completeness relation $\int_{4\pi} F(\hat{\mathbf{e}})\, d\Omega = I$, ensuring that the probabilities of all possible orientations sum to unity and is isotropic $\int e_i\, F(\hat{\mathbf{e}})\, d\Omega = \frac{1}{3}\,\hat{E}_i$.

To evaluate Eq. (18), the POVM $F(\hat{\mathbf{e}})$ is expanded in an irreducible tensor basis constructed from $\hat{\mathbf{e}}$, i.e.,

$$F(\hat{\mathbf{e}}) = \frac{1}{4\pi} I + \frac{1}{4\pi} e_i \hat{E}_i + a_2 Q_{ij}(\hat{\mathbf{e}}) \hat{Q}_{ij} + \cdots \tag{19}$$

Here, $Q_{ij}(\hat{\mathbf{e}}) = e_i e_j - \frac{1}{3}\delta_{ij}$ is the traceless quadrupole and $\hat{Q}_{ij}$ the corresponding rank-2 operator on the orientation space. We also assume that the joint state ϱ has isotropic marginals, meaning that neither the orientation nor the spin subsystem possesses a net vector expectation:

$$\mathrm{Tr}\big[\varrho\,(\hat{E}_i \otimes I)\big] = 0, \qquad \mathrm{Tr}\big[\varrho\,(I \otimes \hat{\sigma}_j)\big] = 0. \tag{20}$$

Substituting Eq. (19) into Eq. (18), we see that the only term in the numerator that can produce a vector quantity is the rank-1 term $\frac{1}{4\pi} e_i \hat{E}_i$. Meanwhile, the scalar and higher-rank terms cannot contract with $\hat{\sigma}_j$ to yield a rank-1 object without a vector available from the state itself, which is excluded by isotropy, thus,

$$\mathrm{Tr}\big\{\varrho\,[F(\hat{\mathbf{e}}) \otimes \hat{\sigma}_j]\big\} = \frac{1}{4\pi} e_i \ \mathrm{Tr}\big[\varrho\,(\hat{E}_i \otimes \hat{\sigma}_j)\big]. \tag{21}$$

Similarly, the denominator of Eq. (18) becomes

$$\mathrm{Tr}\big\{\varrho\,[F(\hat{\mathbf{e}}) \otimes I]\big\} = \frac{1}{4\pi}\ \mathrm{Tr}[\varrho] + a_2 Q_{kl}(\hat{\mathbf{e}})\ \mathrm{Tr}\big[\varrho\,(\hat{Q}_{kl} \otimes I)\big] + \cdots \tag{22}$$

The rank-1 term vanishes because of the assumption that the joint state ϱ has isotropic marginals, Eq. (20), while the scalar term yields a constant $\frac{1}{4\pi}\,\mathrm{Tr}[\varrho]$. For an isotropic orientation marginal, all rank ≥ 1 contributions vanish, so the denominator reduces to the constant $\frac{1}{4\pi}\,\mathrm{Tr}[\varrho]$.

The the orientation-conditioned expectation value of the spin, Eq. (18), thereby simplifies to

$$\langle \sigma_j \rangle_{\hat{\mathbf{e}}} = \ e_i G_{ij} \qquad G_{ij} = \mathrm{Tr}\big[\varrho\,(\hat{E}_i \otimes \hat{\sigma}_j)\big]. \tag{23}$$

If G_{ij} is symmetric, as in the uniaxial case $G_{ij} = G_{ji}$, then the same tensor also governs the spin-conditioned orientation law $\langle E_i \rangle_{\hat{\mathbf{s}}} \propto G_{ij} s_j$, demonstrating that both conditional averages originate from the same correlator G_{ij}.

Indeed, the spin-conditioned expectation value of the molecular orientation can be written analogously as

$$\langle E_i \rangle_{\hat{\mathbf{s}}} = \frac{\mathrm{Tr}\big[\varrho\,(\hat{E}_i \otimes \hat{P}_{\hat{\mathbf{s}}})\big]}{\mathrm{Tr}\big[\varrho\,(I \otimes \hat{P}_{\hat{\mathbf{s}}})\big]}, \tag{24}$$

in which the joint density operator ϱ describes the correlated orientation–spin system. Here, $\hat{P}_{\hat{\mathbf{s}}}$ is the spin projector corresponding to detecting an electron spin oriented along $\hat{\mathbf{s}}$, i.e.,

$$\hat{P}_{\hat{\mathbf{s}}} = \tfrac{1}{2}\big(I + \hat{\mathbf{s}}\cdot\boldsymbol{\sigma}\big), \tag{25}$$

where, $\boldsymbol{\sigma}$ is the vector of Pauli matrices. Substituting $P_{\hat{\mathbf{s}}}$ into Eq. (24), and assuming isotropic marginal states, Eq. (20), we obtain

$$\langle E_i \rangle_{\hat{\mathbf{s}}} = \frac{s_j}{\mathrm{Tr}[\varrho]} G_{ij} = G_{ij} s_j, \qquad G_{ij} = \mathrm{Tr}\big[\varrho\,(\hat{E}_i \otimes \hat{\sigma}_j)\big]. \tag{26}$$

Hence, both the spin-conditioned, Eq. (23), and orientation-conditioned, Eq. (26), averages are governed by the same correlation tensor G_{ij}, reflecting that the observed spin–orientation correlations originate from a single microscopic source - the quantum entanglement encoded in the joint state ϱ.

Orientation-conditioned spin polarization from the correlation tensor

We start from the (uniaxial) spin–orientation correlation tensor

$$G_{ij} = \kappa\big[\mathcal{S}_i\mathcal{S}_j + \gamma\left(|\boldsymbol{\mathcal{S}}|^2\delta_{ij} - \mathcal{S}_i\mathcal{S}_j\right)\big]\,, \tag{27}$$

where $\boldsymbol{\mathcal{S}}$ is the intrinsic molecular-frame pseudovector that sets the uniaxial symmetry of the coupling, κ is a scalar scale factor, and γ is the transverse/longitudinal anisotropy parameter. Indices $i, j \in \{x, y, z\}$ and Einstein summation is implied over repeated indices.

For an *orientation-conditioned* measurement, the mean spin polarization is obtained by contracting G_{ij} with e_j:

$$\langle s_i \rangle_{e_j} \;=\; G_{ij}\, e_j. \tag{28}$$

Substituting Eq. (27) into Eq. (28) we obtain:

$$\begin{aligned}\langle s_i \rangle_{e_j} =& \kappa\big[\mathcal{S}_i(\mathcal{S}_j e_j) + \gamma\left(|\boldsymbol{\mathcal{S}}|^2\delta_{ij}e_j - \mathcal{S}_i\mathcal{S}_j e_j\right)\big] \\ =& \kappa\big\{\mathcal{S}_i\left(\boldsymbol{\mathcal{S}}\cdot\hat{\mathrm{e}}\right) + \gamma\left[|\boldsymbol{\mathcal{S}}|^2 e_i - \mathcal{S}_i\left(\boldsymbol{\mathcal{S}}\cdot\hat{\mathrm{e}}\right)\right]\big\}.\end{aligned} \tag{29}$$

which can be written in vector form as:

$$\langle \hat{\mathrm{s}} \rangle_{\hat{\mathrm{e}}} = \kappa\Big[\left(\boldsymbol{\mathcal{S}}\cdot\hat{\mathrm{e}}\right)\boldsymbol{\mathcal{S}} + \eta\Big(|\boldsymbol{\mathcal{S}}|^2\hat{\mathrm{e}} - \left(\boldsymbol{\mathcal{S}}\cdot\hat{\mathrm{e}}\right)\boldsymbol{\mathcal{S}}\Big)\Big]. \tag{30}$$

Synthetic chiral matter

Quantification of spin-chirality coupling in photoionization requires a system where both electronic chirality and spin-orbit coupling are rigorously accounted. To this end, we construct chiral electronic densities in an Ar atom corresponding to excitation into a chiral superposition of excited states, resolved on the excited electron spin. The eigenstates and associated spin-resolved photoionization dipole matrix elements of Ar atom were calculated using an atomic configuration-interaction singles treatment [37,40,41]:

$$\vec{\boldsymbol{D}}^{M}_{I,\vec{\boldsymbol{k}}^{M},\mu^{M}} \equiv \langle I\Psi^{(-)}_{I,\vec{\boldsymbol{k}},\mu^{M}}|\vec{\boldsymbol{d}}^{M}|\psi_o\rangle \;=\; \langle\psi^{(-)}_{I,\vec{\boldsymbol{k}},\mu^{M}}|\,\langle\chi_{\mu^{M}}|[\hat{h}_S,\theta(r-r_s)]\sqrt{N}\,\langle I|(\hat{H}_0-\epsilon)^{-1}\vec{\boldsymbol{d}}^{M}|\psi_o\rangle\,, \tag{31}$$

In Eq. (31), the volume integral in the matrix element is replaced with a surface integral over a sphere of radius r_s where the exact continuum state is matched to the scattering state in

the asymptotic region [37] and a time integral which has been explicitly evaluated. The resolvent $(\hat{H}_0 - \epsilon)^{-1}$ formally propagates the component of $\vec{\boldsymbol{d}}^M |\psi_o\rangle$ with energy $\epsilon = E_I + k^2/2$ to infinite time, where E_I is the energy of the ion state I, and the projection from the left by $\sqrt{N}\langle I|$ yields an energy-resolved Dyson orbital (N is the number of electrons). The commutator of the scattering Hamiltonian $\hat{h}_S$, i.e., the asymptotic Hamiltonian obeyed by the wave function and the scattering state in the region beyond the matching surface r_s and the Heaviside function $\theta(r - r_s)$ reduces the remaining one-electron volume integral to the surface integral [37].

Chiral spin resolved electronic states in Ar are inspired by a similar spinless chiral superposition in the hydrogen atom [35], and in the case of hydrogenic wave-functions could be represented as:

$$|\psi^{\pm}_{m,\mu}\rangle = \frac{1}{\sqrt{2}} \left(|4p_m, \mu\rangle \pm |4d_m, \mu\rangle \right). \tag{32}$$

Aiming to create analogues of such states in a multielectron system such as the argon atom, we devised an optimization procedure that yields the best approximation to these states (see Appendix A for details).

Bloch vector associated with spin-resolved photoionization

Using perturbation theory, the full spinor electron wave-function at the end of the ionizing pulse is:

$$|\psi\rangle = |\psi_o\rangle + \sum_{I,\mu^M} \int \mathrm{d}\Theta^M_k \, c_{I,\vec{\boldsymbol{k}}^M,\mu^M} |I\Psi^{(-)}_{I,\vec{\boldsymbol{k}}^M,\mu^M}\rangle, \tag{33a}$$

$$c_{I,\vec{\boldsymbol{k}}^M,\mu^M} = i \left(\vec{\boldsymbol{D}}^L_{I,\vec{\boldsymbol{k}}^M,\mu^M} \cdot \vec{\boldsymbol{E}}^L \right), \tag{33b}$$

where, $|\Psi^{(-)}_{I,\vec{\boldsymbol{k}},\mu}\rangle$ are fully spin-orbit coupled continuum states, which are the two components of a spinor-valued scattering solution with opposite projections of spin ($\mu = \pm\frac{1}{2}$) onto the molecular z-axis $\hat{\boldsymbol{\zeta}}$ subject to the orthogonality condition $\langle I_1\Psi^{(-)}_{I_1,\vec{\boldsymbol{k}}_1,\mu_1}|I_2\Psi^{(-)}_{I_2,\vec{\boldsymbol{k}}_2,\mu_2}\rangle = \delta_{I_1,I_2}\delta(\vec{\boldsymbol{k}}_1 - \vec{\boldsymbol{k}}_2)\delta_{\mu_1,\mu_2}$. The ion channel is denoted by I, while $\vec{\boldsymbol{D}}^{L}_{I,\vec{\boldsymbol{k}}^M,\mu^M} = \langle I\Psi^{(-)}_{I,\vec{\boldsymbol{k}},\mu}|\vec{\boldsymbol{d}}^{\boldsymbol{L}}|\psi_0\rangle$ is the transition dipole matrix element, and $\vec{\boldsymbol{E}}^{L}$ is the light field.

We now consider the full density operator describing the spin and spatial degrees of freedom for ionization into the final photoelectron momentum $k = \sqrt{2E}$ and (degenerate) ion channels I (fixed by the energy conservation):

$$\hat{\varrho}^M = \sum_{I,I'}\int d\Theta^M_k \int d\Theta^M_{k'} \sum_{\mu_1,\mu_2} c_{I,\vec{\boldsymbol{k}},\mu_1} c^*_{I',\vec{\boldsymbol{k}}',\mu_2} |I\Psi_{I,\vec{\boldsymbol{k}}',\mu_1}\rangle\langle\Psi_{I,\vec{\boldsymbol{k}},\mu_2}I'|. \tag{34}$$

To obtain the reduced spin-space density matrix, we perform a partial trace over the spatial continuum states and (degenerate) ionization channels:

$$\varrho^M_{\mu_1,\mu_2} = \mathrm{Tr}_{(\text{spatial+channels})}(\hat{\varrho}^M) = \sum_I \int d\Theta^M_k \langle I\Psi_{I,\vec{\boldsymbol{k}},\mu_1}|\hat{\varrho}^M|I\Psi_{I,\vec{\boldsymbol{k}},\mu_2}\rangle. \tag{35}$$

Using Eqs. (34) and (35), we obtain:

$$\varrho^M_{\mu_1,\mu_2} = \sum_I \int d\Theta^M_k c_{I,\vec{\boldsymbol{k}},\mu_1} c^*_{I,\vec{\boldsymbol{k}},\mu_2}, \tag{36}$$

which follows from the orthogonality condition.

A possible way of introducing the Bloch vector describing spin orientation of a two-level spin $1/2$ system defined as $\vec{\boldsymbol{P}} \equiv \mathrm{Tr}\left(\varrho^M \hat{\boldsymbol{\sigma}}^M\right)$ is to use ϱ^M with elements given by Eq. (36). In this case, the Bloch vector would depend on the properties of the laser field via $c_{I,\vec{\boldsymbol{k}},\mu_1}, c_{I,\vec{\boldsymbol{k}},\mu_2}$. However,

such object does not characterize enantio-sensitive spin orientation locking as it follows from first principles derivation of spin-orientation locking exposed in the last subsection of Methods.

We now introduce the photoionization Bloch vector $\vec{\boldsymbol{S}}^M$ by averaging $\varrho^M_{\mu_1,\mu_2}$ over random molecular orientations, i.e.,

$$\int d\rho\, \varrho^M_{\mu_1,\mu_2} = \sum_I \int d\Theta^M_k \left[\int d\rho \left(\vec{\boldsymbol{D}}^L_{I,\vec{\boldsymbol{k}}^M,\mu_1^M} \cdot \vec{\boldsymbol{E}}^L \right) \left(\vec{\boldsymbol{D}}^{L*}_{I,\vec{\boldsymbol{k}}^M,\mu_2^M} \cdot \vec{\boldsymbol{E}}^{L*} \right) \right] = \frac{1}{3} |\vec{\boldsymbol{E}}^L|^2 \tilde{\varrho}^M_{\mu_1,\mu_2} \tag{37a}$$

$$\tilde{\varrho}^M_{\mu_1,\mu_2} = \sum_I \int d\Theta^M_k \left(\vec{\boldsymbol{D}}^M_{I,\vec{\boldsymbol{k}}^M,\mu_1} \cdot \vec{\boldsymbol{D}}^{M*}_{I,\vec{\boldsymbol{k}}^M,\mu_2} \right). \tag{37b}$$

Normalizing $\tilde{\varrho}^M_{\mu_1,\mu_2}$ in a standard way to its trace $\mathrm{Tr}[\tilde{\varrho}^M] = S_0$, where S_0 is the total ionization rate:

$$S_0 = \sum_I \left[\int d\Theta^M_k \left(\left| \vec{\boldsymbol{D}}^M_{I,\vec{\boldsymbol{k}}^M,\frac{1}{2}} \right|^2 + \left| \vec{\boldsymbol{D}}^M_{I,\vec{\boldsymbol{k}}^M,-\frac{1}{2}} \right|^2 \right) \right] \tag{38}$$

we can write in the following equivalent form:

$$\frac{\tilde{\varrho}^M}{\mathrm{Tr}[\tilde{\varrho}^M]} = \frac{1}{2} \left(\mathbb{I} + \vec{\boldsymbol{S}}^M \cdot \hat{\boldsymbol{\sigma}}^M \right). \tag{39}$$

Here, $\vec{\boldsymbol{S}}^M$ is the photo-ionization Bloch pseudovector in real space

$$\vec{\boldsymbol{S}}^M = \frac{1}{S_0} \mathrm{Tr} \left(\tilde{\varrho}^M \hat{\boldsymbol{\sigma}}^M \right). \tag{40}$$

$\vec{\boldsymbol{S}^M}$ is an intrinsic molecular property invariant under rotations of the spin quantization axis provided that these rotations are applied consistently to both the density matrix $\tilde{\varrho}^M$ and the spin operator $\hat{\boldsymbol{\sigma}}^M$.

Quantifying spin-orientation locking

The spin-resolved ionization rate for a given orientation is obtained by projecting the full wavefunction Eq. (33) onto the scattering and ionic states onto the spin detection axis $\hat{\boldsymbol{s}}^L$ with energy

$\mathcal{E}$, i.e.,

$$W^M(k^M, \hat{\boldsymbol{s}}^M, \rho) = \langle\psi|\hat{\mathsf{P}}_{\mathcal{E}}|\psi\rangle = \int d\Theta_k^M W^M(\hat{\boldsymbol{k}}^M, \hat{\boldsymbol{s}}^M, \rho) \tag{41a}$$

$$\hat{\mathsf{P}}_{\mathcal{E}} = \sum_{I,\mu_1,\mu_2} \int d\Theta_k^M |I\Psi^{(-)}_{I,\vec{k},\mu_1}\rangle \left[\frac{\mathbb{I} + \hat{\boldsymbol{s}}^L \cdot \hat{\boldsymbol{\sigma}}^L}{2}\right]_{\mu_2,\mu_1} \langle I\Psi^{(-)}_{I,\vec{k},\mu_2}|, \tag{41b}$$

where, $W^M(\hat{\boldsymbol{k}}^M, \hat{\boldsymbol{s}}^M, \rho)$ is the the momentum- and spin-resolved rate. Substituting Eq. (33) into Eq. (41), and performing the necessary operations, we obtain

$$W^M(\hat{\boldsymbol{k}}^M, \hat{\boldsymbol{s}}^M, \rho) = \frac{1}{2} \sum_{I,\mu_1^M,\mu_2^M} \left(\vec{\boldsymbol{D}}^{L*}_{I,\vec{\boldsymbol{k}}^M,\mu_1^M} \cdot \vec{\boldsymbol{E}}^{L*}\right) \left(\vec{\boldsymbol{D}}^{L}_{I,\vec{\boldsymbol{k}}^M,\mu_2^M} \cdot \vec{\boldsymbol{E}}^{L}\right) \left(\delta_{\mu_1^M,\mu_2^M} + \hat{\boldsymbol{s}}^M \cdot \hat{\boldsymbol{\sigma}}^M_{\mu_2^M,\mu_1^M}\right), \tag{42}$$

where, we introduced the vector $\hat{\boldsymbol{\sigma}}^L_{\mu,\nu} = \langle\chi_\mu|\hat{\boldsymbol{\sigma}}^M|\chi_\nu\rangle$.

Equation (42) fixes the photoelectron momentum and spin-detection axis in the molecular and laboratory frame, respectively. By doing so, the transition dipole matrix element in the molecular frame $\vec{\boldsymbol{D}}^M_{I,\vec{\boldsymbol{k}}^M,\mu^M}$ will not have any argument that depends on the orientation ρ, and can therefore be trivially rotated into the lab frame:

$$\begin{aligned}\vec{\boldsymbol{D}}^L_{I,\vec{\boldsymbol{k}}^M,\mu^M} =& \langle I\Psi^{(-)}_{I,\vec{\boldsymbol{k}}^M,\mu^M}|\vec{\boldsymbol{d}}^L|\psi_o\rangle = \langle I\Psi^{(-)}_{I,\vec{\boldsymbol{k}}^M,\mu^M}|R_\rho\vec{\boldsymbol{d}}^M|\psi_o\rangle \\ =& R_\rho\langle I\Psi^{(-)}_{I,\vec{\boldsymbol{k}}^M,\mu^M}|\vec{\boldsymbol{d}}^M|\psi_o\rangle = R_\rho\vec{\boldsymbol{D}}^M_{I,\vec{\boldsymbol{k}}^M,\mu^M}.\end{aligned} \tag{43}$$

Meanwhile, by fixing the spin-detection axis in the lab frame, the spin projection operator $\hat{\mathsf{P}}_{\hat{\boldsymbol{s}}} = \left(\mathbb{I} + \hat{\boldsymbol{s}}^L \cdot \hat{\boldsymbol{\sigma}}^L\right)/2$ essentially rotates the direction of photoelectron spin from the molecular to the laboratory frame, then projects it to the spin-detection axis $\hat{\boldsymbol{s}}^L$:

$$\hat{\boldsymbol{s}}^L \cdot \hat{\boldsymbol{\sigma}}^L_{\mu_1^M,\mu_2^M} = \hat{\boldsymbol{s}}^L \cdot \langle\chi_{\mu_1^M}|R_\rho\hat{\boldsymbol{\sigma}}^M|\chi_{\mu_2^M}\rangle = \hat{\boldsymbol{s}}^L \cdot R_\rho\langle\chi_{\mu_1^M}|\hat{\boldsymbol{\sigma}}^M|\chi_{\mu_2^M}\rangle = \hat{\boldsymbol{s}}^L \cdot \left(R_\rho\hat{\boldsymbol{\sigma}}^M_{\mu_1^M,\mu_2^M}\right). \tag{44}$$

Equation (42) can thus be written as

$$
\begin{aligned}
&W^M(\hat{\boldsymbol{k}}^M, \hat{\boldsymbol{s}}^M, \rho) \\
&= \frac{1}{2} \sum_{I,\mu_1^M,\mu_2^M} \left[\left(R_\rho \vec{\boldsymbol{D}}^{M*}_{I,\vec{\boldsymbol{k}}^M,\mu_1^M} \right) \cdot \vec{\boldsymbol{E}}^{L*} \right] \left[\left(R_\rho \vec{\boldsymbol{D}}^{M}_{I,\vec{\boldsymbol{k}}^M,\mu_2^M} \right) \cdot \vec{\boldsymbol{E}}^{L} \right] \left\{ \delta_{\mu_1^M,\mu_2^M} + \left[\hat{\boldsymbol{s}}^L \cdot \left(R_\rho \hat{\boldsymbol{\sigma}}^M_{\mu_2^M,\mu_1^M} \right) \right] \right\}
\end{aligned}
\tag{45}
$$

The vectors that appear on the right-hand side of Eq. (45) can now be grouped into two sets: (i) vectors that are fixed in the molecular frame such as the dipole transition vectors $\vec{\boldsymbol{D}}^M_{I,\vec{\boldsymbol{k}}^M,\mu^M}$, photoelectron momentum $\vec{\boldsymbol{k}}^M$, and photoelectron spin expectation value $\hat{\boldsymbol{\sigma}}^M_{\mu_1^M,\mu_2^M}$, and (ii) vectors that are fixed in the laboratory frame such as spin detection axis $\hat{\boldsymbol{s}}^L$ and the electric field $\vec{\boldsymbol{E}}^L$. This will then allow us to use the technique in Ref. [42] in evaluating the orientation averaging $\int d\rho$ such that the resulting quantity can be expressed as $\sum_{ij} g_i M_{ij} f_j$, where, g_i and f_i are rotational invariants that are constructed from the two sets of vectors and M_{ij} is the coupling between the two rotational invariants.

Let us now consider the spin-conditioned expectation value of the molecular orientation under isotropic illumination:

$$
\left\langle \langle \hat{\boldsymbol{e}}^L \rangle_{\hat{\boldsymbol{s}}^L} \right\rangle^{\text{iso}}_{\rho} \equiv \frac{\int d\Theta_k^M \int d\Theta_p \int d\rho W^M(\hat{\boldsymbol{k}}^M, \hat{\boldsymbol{s}}^M, \rho) \vec{\boldsymbol{e}}^L}{\int d\Theta_s^L \int d\Theta_k^M \int d\Theta_p \int d\rho W^M(\hat{\boldsymbol{k}}^M, \hat{\boldsymbol{s}}^M, \rho)}. \tag{46}
$$

Instead of a single direction that characterizes the direction of polarization, e.g., $\hat{\boldsymbol{x}}^L$, we introduce the light field

$$
\vec{\boldsymbol{E}}^L_p = E^L_\omega \left(\sin\theta_p \cos\varphi_p \hat{\boldsymbol{x}}^L + \sin\theta_p \sin\varphi_p \hat{\boldsymbol{y}}^L + \cos\theta_p \hat{\boldsymbol{z}}^L \right) \tag{47}
$$

Combining Eqs. (45)-(47), then averaging over all molecular orientation $\int d\rho$, and orientations of

the field $\int d\Theta_p$, we finally obtain

$$\left\langle \langle \hat{\boldsymbol{e}}^L \rangle_{\hat{\boldsymbol{s}}^L} \right\rangle_\rho^{\text{iso}} = \frac{1}{3S_0} (\vec{\boldsymbol{S}}^M \cdot \vec{\boldsymbol{e}}^M) \hat{\boldsymbol{s}}^L \tag{48}$$

The product $\vec{\boldsymbol{S}}^M \cdot \vec{\boldsymbol{e}}^M$ is maximal when $\vec{\boldsymbol{S}}^M \parallel \vec{\boldsymbol{e}}^M$, thus, we can identify $\vec{\boldsymbol{S}}^M$ with the molecular axis that becomes oriented. Now, consider a unit polar vector $\hat{\boldsymbol{e}}^M$ pointing in the direction of the Bloch vector $\hat{\boldsymbol{e}}^M \parallel \hat{\boldsymbol{S}}^M$ in a given enantiomer. The orientation averaged value of $\langle \hat{\boldsymbol{e}}^L \rangle$ is

$$\left\langle \langle \hat{\boldsymbol{e}}^L \rangle_{\hat{\boldsymbol{s}}^L} \right\rangle_\rho^{\text{iso}} = \frac{\nu}{3S_0} |\vec{\boldsymbol{S}}^M| \hat{\boldsymbol{s}}^L. \tag{49}$$

where, $\nu = \pm 1$ for opposite enantiomers.

A similar straightforward calculation for a light field polarized along $\hat{\boldsymbol{\epsilon}}^L$ will yield

$$\left\langle \langle \hat{\boldsymbol{e}}^L \rangle_{\hat{\boldsymbol{s}}^L} \right\rangle_\rho = \frac{1}{5S_0} \left[\left(2\vec{\boldsymbol{S}}^M + \vec{\boldsymbol{S}}'^M \right) \right] \hat{\boldsymbol{s}}^L - \frac{1}{5S_0} \left[\left(\vec{\boldsymbol{S}}^M + 3\vec{\boldsymbol{S}}'^M \right) \right] (\hat{\boldsymbol{s}}^L \cdot \hat{\boldsymbol{\epsilon}}^L) \hat{\boldsymbol{\epsilon}}^L. \tag{50}$$

Equation (50) now presents two detection geometries: (i) orthogonal $\hat{\boldsymbol{s}}^L \perp \hat{\boldsymbol{\epsilon}}^L$, and (ii) collinear $\hat{\boldsymbol{s}}^L \parallel \hat{\boldsymbol{\epsilon}}^L$ which results to different axes of molecular orientation as shown in Eqs. (13) and (14), respectively. Here, the additional vector $\vec{\boldsymbol{S}}'^M$ has the form

$$\vec{\boldsymbol{S}}'^M = \frac{1}{S_0} \text{Re} \left[\sum_{I,\mu_1^M,\mu_2^M} \int d\Theta_k^M \left(\vec{\boldsymbol{D}}^{M*}_{I,\vec{\boldsymbol{k}}^M,\mu_1^M} \cdot \hat{\boldsymbol{\sigma}}^M_{\mu_2^M,\mu_1^M} \right) \vec{\boldsymbol{D}}^M_{I,\vec{\boldsymbol{k}}^M,\mu_2^M} \right], \tag{51}$$

which presents the directional bias induced by the well-defined direction of light polarization $\hat{\boldsymbol{\epsilon}}^L$.

Estimating the degree of orientation

An estimate of the number of 'head' $N_{+\hat{\boldsymbol{s}}}$ and 'tail' $N_{-\hat{\boldsymbol{s}}}$ molecules corresponding to the averaged angle $\langle \hat{\boldsymbol{e}}^L \cdot \hat{\boldsymbol{s}}^L \rangle = \langle \cos\beta \rangle$ between the vector $\hat{\boldsymbol{e}}^L$ and "target" orientation axis $\hat{\boldsymbol{s}}^L$, can be performed

by adopting the methods of Ref. [43] to model the angular distribution of oriented molecules. Let

$$\Psi(\theta,\varphi) = a_0 Y_{0,0}(\theta,\varphi) + b_0 Y_{1,0}(\theta,\varphi) + \frac{b_-}{\sqrt{2}}[Y_{1,-1}(\theta,\varphi) - Y_{1,1}(\theta,\varphi)] + i\frac{b_+}{\sqrt{2}}[Y_{1,-1}(\theta,\varphi) + Y_{1,1}(\theta,\varphi)], \tag{52}$$

where, $|a_0|^2 + |b_0|^2 + |b_-|^2 + |b_+|^2 = 1$. Without loss of generality, let us consider the spin detection axis $\hat{\boldsymbol{s}}^L \parallel \hat{\boldsymbol{z}}^L$ such that

$$N_{+\hat{\boldsymbol{z}}} = \int_0^{2\pi} d\varphi \int_0^{\pi/2} d\theta \sin\theta |\Psi(\theta,\varphi)|^2 \cos\theta = \frac{1}{2}\left(1 + \frac{3}{2}\langle \hat{\boldsymbol{e}}^L \cdot \hat{\boldsymbol{s}}^L \rangle\right) \tag{53}$$

$$N_{-\hat{\boldsymbol{z}}} = = 1 - N_{+\hat{\boldsymbol{z}}}. \tag{54}$$

For the case of isotropic illumination of randomly oriented electronic states, Fig. 3, this corresponds to $N_{+\hat{\boldsymbol{z}}} \approx 0.6$ for $\langle \hat{\boldsymbol{e}}^L \cdot \hat{\boldsymbol{s}}^L \rangle \approx 0.13$.

O.S., A.F. O. and P.C.F. acknowledge ERC-2021-AdG project ULISSES, grant agreement No 101054696. Views and opinions expressed are however those of the author(s) only and do not necessarily reflect those of the European Union or the European Research Council. Neither the European Union nor the granting authority can be held responsible for them. A.F.O. acknowledges funding from the Royal Society URF/R1/201333, URF/ERE/210358, and URF/ERE/231177 and from the Deutsche Forschungsgemeinschaft (DFG, German Research Foundation) - 543760364.

Appendices

A Chiral superpositions of Argon excited states

The excited states of argon have good quantum numbers J and M_J, when considering spin–orbit interaction:

$$\hat{H}_0 \left|w\right\rangle = E_w \left|w\right\rangle , \quad \hat{\vec{J}}^2 \left|w\right\rangle = J(J+1) \left|w\right\rangle , \quad \hat{J}_z \left|w\right\rangle = M_J \left|w\right\rangle . \tag{55}$$

In a close-coupling description of the excited states, the active electron is *entangled* with the ion. In the particle–hole basis employed in configuration-interaction singles [40,41], the excited states have contributions from multiple ion channels:

$$\left|w\right\rangle = \sum_i \hat{\mathcal{A}} \left(\hat{a}_i \left|\Phi_0\right\rangle\right) \left|\chi_i\right\rangle , \tag{56}$$

where $\left|\Phi_0\right\rangle$ is the Hartree–Fock reference state (the ground state), $\hat{a}_i$ annihilates the ith occupied orbital, $\left|\chi_i\right\rangle$ is the channel-specific orbital for the excited or free electron, and $\hat{\mathcal{A}}$ is the antisymmetrization operator. $\hat{a}_i \left|\Phi_0\right\rangle$ is thus an approximation to the state of the ion (Koopmans approximation), and the orbitals of $\hat{a}_i \left|\Phi_0\right\rangle$ and $\left|\chi_i\right\rangle$ are expanded in the $\ell j m_j$ basis, wherein the spin–orbit interaction is diagonal. In our calculations, relativistic effects (of which the spin–orbit interaction is one), are treated using a relativistic effective-core potential [44] (there are alternative approaches described in the literature [45–47], but for our purposes, the present approach is more suitable).

For each excited state $\left|w\right\rangle$, we may compute the ionization dipole matrix elements $\langle I\vec{\boldsymbol{k}}m_s|\hat{d}|w\rangle$, using a surface-flux technique [37,40], and they are resolved on the ion state I and the photoelectron

state in terms of the magnitude $k = |\vec{k}|$ of the linear momentum, the angular distribution in terms of the orbital angular momentum $(\ell m_\ell)_{\vec{k}}$, and the spin m_s.

We however desire the ionization dipole matrix elements starting from a chiral superposition of states which as far as possible resemble factorized one-electron excited states characterized by $n\ell m_\ell s m_s$, i.e. our desired initial wavefunction is given by

$$|\Psi\rangle = |\Psi_{\text{ion}}\rangle \left[\sum_i f_i \, |(n\ell m_\ell s m_s)_i\rangle \right] \stackrel{\text{def}}{=} |\Psi_{\text{ion}}\rangle \sum_i f_i \, |k_i\rangle \,, \tag{57}$$

where the ionic state $|\Psi_{\text{ion}}\rangle$ is shared between all terms in the expansion, and the expansion coefficients f_i may be chosen at will. In the second step, we have introduced a short-hand notation for the state of the electron.

To achieve this goal, we proceed in two steps:

1. Find linear combinations of the true excited states $|w\rangle$ that are approximately factorized into an ionic part and an electronic part:

$$|\Phi_i\rangle \approx |\Phi_{\text{ion},i}\rangle \, |k_i\rangle \,. \tag{58}$$

   There will be multiple such approximate factorizations, since there are multiple ionization channels. Below, we discuss how we try to find the "optimal" ones.

2. Given a set $\{|k_i\rangle \, , a_i\}$, try to find linear combinations of the factorized states (58), that simultaneously are as close to the desired chiral superposition as possible, while still maintaining maximum overlap of the ionic wavefunction, since that increases the purity of the state.

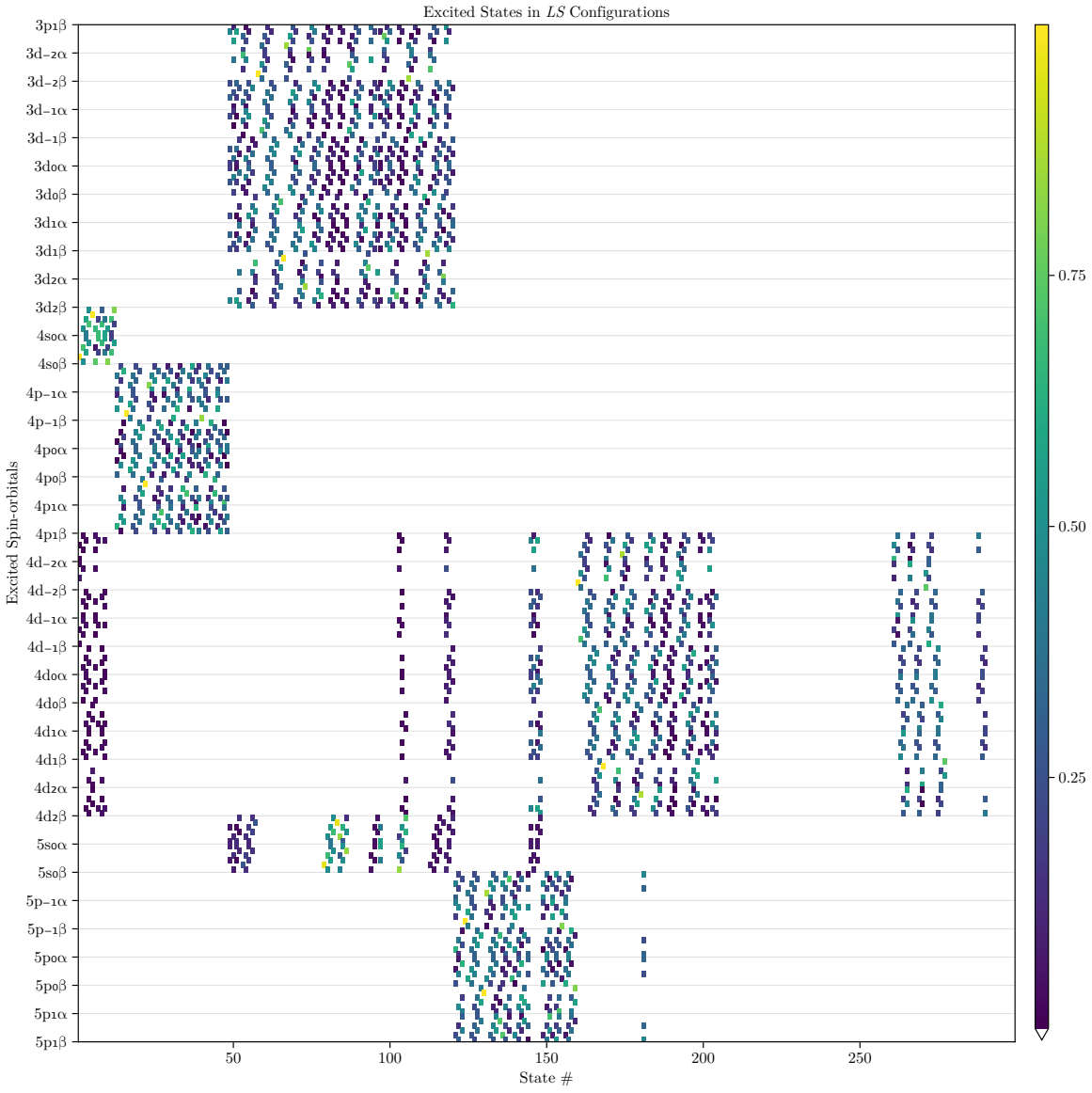

Figure 5: Overlaps between excited states and spin-configurations, i.e. uncoupled configurations of spin-orbitals in the $n\ell m_\ell s m_s$ basis. The spin-configurations (the y axis) are ordered by the quantum numbers of the excited spin-orbital, given as labels pertaining to the block immediately above them. It is clearly visible that this overlap matrix is mostly composed of disjoint blocks, where the excited states are accurately classified by $n\ell$ of the excited spin-orbital.

State Factorization by Block Diagonalization in Orthogonal Subspaces We define the matrix B with matrix elements $b_{vw} \overset{\text{def}}{=} \langle v|w\rangle$, which is the projection of the true excited state $|w\rangle$ given by (55) on the *uncoupled* configuration $|v\rangle$ in the $\ell m_\ell s m_s$ basis. We may permute the rows and columns of the matrix B, such that it consists of mostly disjoint blocks B_b, which we can transform separately (see Fig. 5). This is possible since the quantum numbers of the excited electron are *almost* good quantum numbers. E.g. a $4\mathrm{s}_0\alpha$ state, will contain contributions from $4\mathrm{d}_{m_\ell}\alpha$ configurations, but they will be of less importance, compared to the dominant configurations.

The rows in each block B_b are ordered such that they are grouped by the excited orbital, and we then wish to apply a transformation to B_b such that it becomes approximately block diagonal, i.e. we find expansions for states with a particular excited orbital (in the $\ell m_\ell s m_s$ basis) in terms of the true excited states (in the $\ell j m_j$ basis). This achieves the approximate factorization (58), thereby disentangling the states. It will however introduce an energy spread, i.e. the factorized states are no longer stationary states of the Hamiltonian.

We consider without loss of generality a case with two different excited orbitals $|k_p\rangle$ and $|k_q\rangle$ (e.g. $4\mathrm{s}_0\alpha$ and $4\mathrm{s}_0\beta$), and drop the b subscript for brevity. The overlap matrix (within this block) is then given by

$$B = (\hat{P} + \hat{Q})B(\hat{P} + \hat{Q}), \tag{59}$$

where $\hat{P}$ projects on the configurations containing $|k_p\rangle$ and $\hat{Q}$ on configurations containing $|k_q\rangle$.

Within the chosen space, $\hat{P} + \hat{Q} = \hat{\mathbf{1}}$. We wish to find a unitary matrix U, such that

$$\begin{cases} \hat{P}UB\hat{Q} &= 0, \\ \hat{Q}UB\hat{P} &= 0, \end{cases} \tag{60}$$

i.e. a block-diagonalizing transform. We will not be able to achieve this identically, therefore we formulate it as a minimization problem:

$$\begin{aligned} &\min_U \|\hat{P}UB\hat{Q}\|^2 + \|\hat{Q}UB\hat{P}\|^2 \\ &\text{such that } U^\dagger U = \hat{\mathbf{1}}. \end{aligned} \tag{61}$$

Its equivalent Lagrangian formulation, incorporating the unitarity constraint on U using a Lagrangian multiplier λ, is given by

$$\begin{aligned} \hat{L} &= \mathrm{tr}\Big(\hat{Q}^\dagger B^\dagger U^\dagger \hat{P}^\dagger \hat{P} U B \hat{Q}\Big) + \mathrm{tr}\Big(\hat{P}^\dagger B^\dagger U^\dagger \hat{Q}^\dagger \hat{Q} U B \hat{P}\Big) + \lambda[\mathrm{tr}\big(U^\dagger U\big) - 1] \\ &= \mathrm{tr}\Big(\hat{Q}^\dagger B^\dagger U^\dagger \hat{P} U B \hat{Q}\Big) + \mathrm{tr}\Big(\hat{P}^\dagger B^\dagger U^\dagger \hat{Q} U B \hat{P}\Big) + \lambda[\mathrm{tr}\big(U^\dagger U\big) - 1] \\ &= \mathrm{tr}\Big(B\hat{Q}B^\dagger U^\dagger \hat{P} U\Big) + \mathrm{tr}\Big(B\hat{P}B^\dagger U^\dagger \hat{Q} U\Big) + \lambda[\mathrm{tr}\big(U^\dagger U\big) - 1], \end{aligned} \tag{62}$$

where we have used the cyclic property of the trace operation, the fact that $\hat{P}^\dagger \hat{P} = \hat{P}^2 = \hat{P}$, and similarly for $\hat{Q}$. Variation of $\hat{L}$ with respect to $U^\dagger$, and λ, respectively, yields

$$\begin{aligned} \delta_{U^\dagger} \hat{L} &= B\hat{Q}B^\dagger \hat{P} U + B\hat{P}B^\dagger \hat{Q} U + \lambda U = (B\hat{Q}B^\dagger \hat{P} + B\hat{P}B^\dagger \hat{Q} + \lambda \hat{\mathbf{1}})U, \\ \delta_\lambda \hat{L} &= U^\dagger U - \hat{\mathbf{1}}, \end{aligned} \tag{63}$$

which we recognize as an eigenvalue problem. The minimization problem (62) may be solved using any standard non-linear solver; its variation (63) can be used to improve convergence. In our implementation, however, we employ Riemannian manifold optimization [48] of the minimization problem (61) as-is; the matrix U is required to stay on the *Stiefel* manifold, i.e. the matrix manifold

of matrices with mutually orthonormal columns. In Fig. 6, the optimized U is shown, together with the transformed overlap matrix UB.

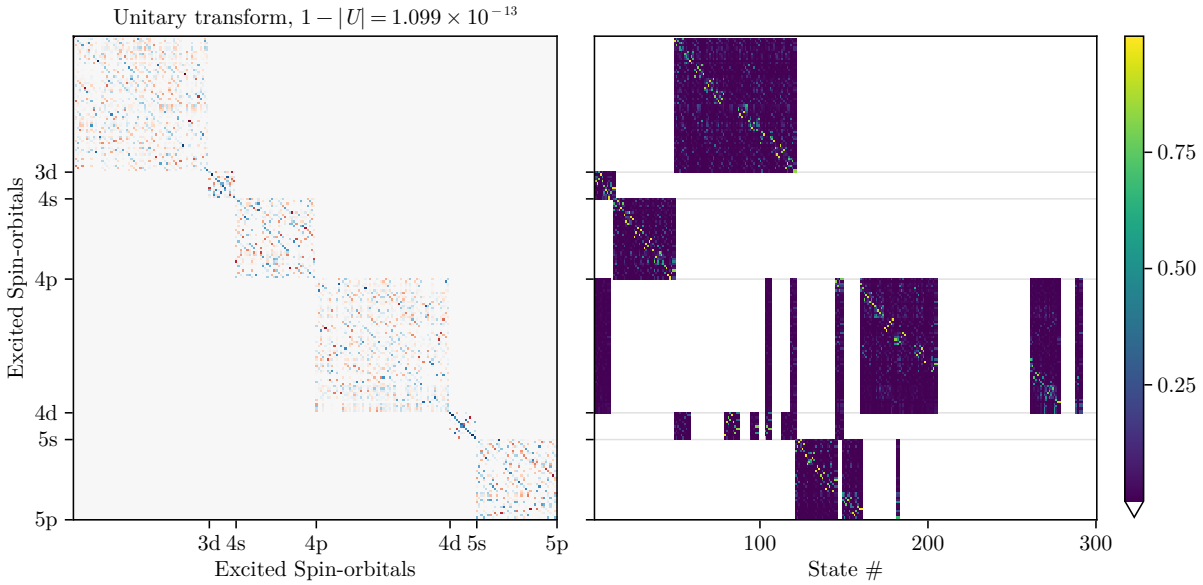

Figure 6: The left panel shows the optimized unitary transform matrix U. The right panel shows the overlap matrix UB between rotated excited states and the spin-configurations, again grouped by the excited spin-orbitals.

With this method, we are able to achieve factorizations that to $\geq 80\,\%$ have the excited electron in the desired spin-orbital $n\ell m_\ell s m_s$, with some residual contamination from other states; see Fig. 7 for the subspace of $4\mathrm{p}$ states. The energy spread is typically small: $(\langle E^2\rangle - \langle E\rangle^2)^{1/2} \lesssim 10^{-2}\langle E\rangle$, with the excited states of interest having energies $\langle E\rangle \gtrsim 0.4\,\mathrm{Ha}$.

Deriving Chiral Superpositions As we saw above (e.g. in Fig. 7), there are multiple states that have the excited electron in the same spin-orbital $|k_i\rangle$. Any of these states may be written as a

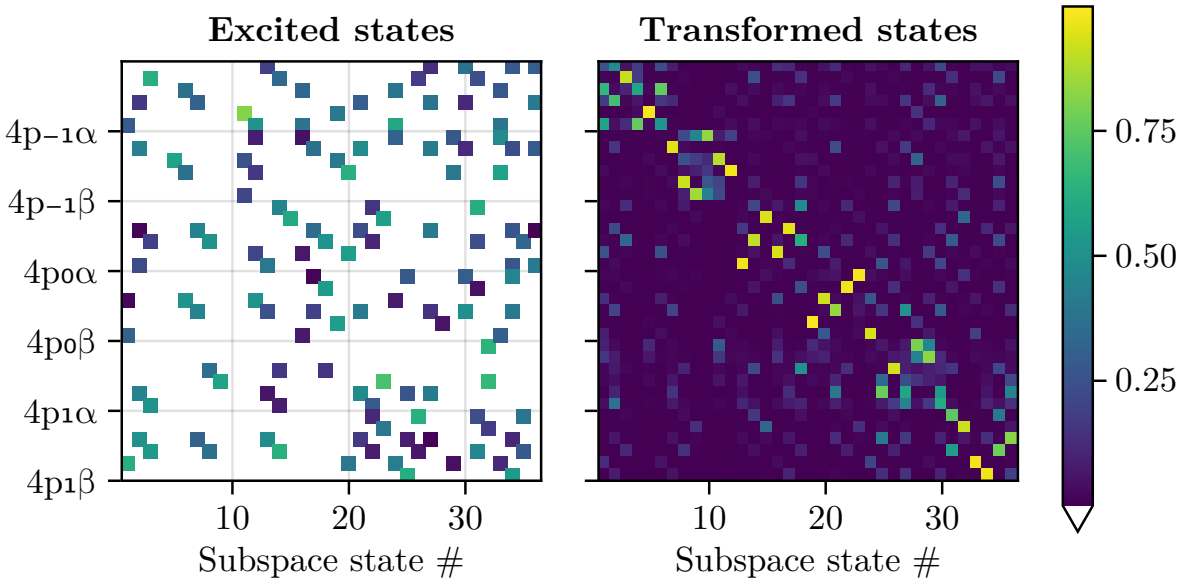

Figure 7: The left panel shows the overlaps between the excited states which are dominated by excited electrons in 4p orbitals, resolved on the individual spin-orbitals. The right panel the resultant states after applying the unitary transform U within this subspace. As can be seen, the block-diagonalization is not perfect. Additionally, we have multiple transformed states for each spin-orbital.

linear combination of the true excited states (55):

$$|\Phi_i\rangle_j = \sum_w c_{jw}^{(i)} |w\rangle = \hat{\mathcal{A}} \left[\sum_w c_{jw}^{(i)} \hat{a}_{k_i} |w\rangle \right] |k_i\rangle \quad \Longrightarrow \left| \vec{\Phi}_i \right\rangle = C_i |\vec{w}\rangle = \hat{\mathcal{A}} \left[C_i \hat{a}_{k_i} |\vec{w}\rangle \right] |k_i\rangle \,, \tag{64}$$

where $|\Phi_i\rangle_j$ is the jth state with the excited electron in the spin-orbital $|k_i\rangle$, $c_{jw}^{(i)}$ the corresponding expansion coefficient for the true eigenstate $|w\rangle$. We also introduce the vector notation $\left|\vec{\Phi}_i\right\rangle^T \overset{\text{def}}{=} \begin{bmatrix} |\Phi_i\rangle_1 & |\Phi_i\rangle_2 & \dots \end{bmatrix}^T$, and similarly for $|\vec{w}\rangle$. C_i are the corresponding expansion coefficients arranged into a matrix. In the second step we have written the states on the factorized form (58).

If we now wish to create a factorized chiral superposition of the excited electron, i.e. we wish to define our initial state according to

$$|\Psi_0\rangle = |\Psi_{\text{ion}}\rangle \sum_i f_i |k_i\rangle \,, \tag{65}$$

for every $|k_i\rangle$ we need to make a linear combination of the possible $|\Phi_i\rangle_j$ such that the ion degrees-of-freedom maximally overlap; otherwise the factorization (65) does not hold. Symbolically, we write this as

$$\left| \vec{g}_i \cdot \vec{\Phi}_i \right\rangle = \vec{g}_i^H C_i |\vec{w}\rangle = \hat{\mathcal{A}} \left[\vec{g}_i^H C_i \hat{a}_{k_i} |\vec{w}\rangle \right] |k_i\rangle \,. \tag{66}$$

To achieve the desired factorized state (65), we thus have to solve the following maximization problem:

$$\begin{aligned} &\max_G \left[\vec{g}_i^H C_i \hat{a}_{k_i} |\vec{w}\rangle \right]^H \left[\vec{g}_j^H C_j \hat{a}_{k_j} |\vec{w}\rangle \right] = \max_G \left[\langle \vec{w}| \hat{a}_{k_i}^\dagger C_i^H \vec{g}_i \right] \left[\vec{g}_j^H C_j \hat{a}_{k_j} |\vec{w}\rangle \right], \\ &\text{such that } \|\vec{g}_i\|^2 = 1, \forall i, \end{aligned} \tag{67}$$

where the ith column of the matrix G is the vector $\vec{g}_i$.

B Quantifying spin-orientation locking

Using perturbation theory, the full spinor valued electron wave-function at the end of the ionizing pulse can be written as

$$|\psi\rangle = |\psi_o\rangle + \sum_{I,\mu^M} \int d\Theta_k^M \, c_{I,\vec{\boldsymbol{k}}^M,\mu^M} |I\Psi^{(-)}_{I,\vec{\boldsymbol{k}}^M,\mu^M}\rangle, \tag{68a}$$

$$c_{I,\vec{\boldsymbol{k}}^M,\mu^M} = i\left(\vec{\boldsymbol{D}}^L_{I,\vec{\boldsymbol{k}}^M,\mu^M} \cdot \vec{\boldsymbol{E}}^L\right) \tag{68b}$$

where $|\psi_o\rangle$ is the ground state of the molecule, I denotes the ionic channel, $|\Psi^{(-)}_{I,\vec{\boldsymbol{k}}^M,\mu^M}\rangle$ is the fully spin-coupled continuum state with momentum $\vec{\boldsymbol{k}}^M$. The transition dipole matrix element in the laboratory frame is $\vec{\boldsymbol{D}}^L_{I,\vec{\boldsymbol{k}}^M,\mu^M} \equiv \langle I\Psi^{(-)}_{I,\vec{\boldsymbol{k}}^M,\mu^M}|\vec{\boldsymbol{d}}^L|\psi_o\rangle$ (see Eq.(31) for details), and the laser field is $\vec{\boldsymbol{E}}^L$.

The spin and momentum resolved photoionization rate for a given orientation is obtained by projecting onto the scattering and ionic states with fixed total energy $\mathcal{E}$ by taking the contributions of the spin-up and down photoelectrons along the spin-detection axis $\hat{\boldsymbol{s}}^L$ as well as final ion states via the projector

$$\hat{\mathsf{P}} = \sum_{I,\mu_1^M,\mu_2^M} |I\Psi^{(-)}_{I,\vec{\boldsymbol{k}}^M,\mu_1^M}\rangle \left[\frac{\mathbb{I} + \hat{\boldsymbol{s}}^M \cdot \hat{\boldsymbol{\sigma}}^M}{2}\right]_{\mu_2^M,\mu_1^M} \langle I\Psi^{(-)}_{I,\vec{\boldsymbol{k}}^M,\mu_2^M}|. \tag{69}$$

Here, the spin-detection axis is rotated from the laboratory to the molecular frame $\hat{\boldsymbol{s}}^L = R_\rho \hat{\boldsymbol{s}}^M$, and $\hat{\boldsymbol{\sigma}}^M$ is the vector of Pauli spin matrices

$$\hat{\boldsymbol{\sigma}}^M = \begin{bmatrix} 0 & 1 \\ 1 & 0 \end{bmatrix} \hat{\boldsymbol{\xi}}^M + \begin{bmatrix} 0 & -i \\ i & 0 \end{bmatrix} \hat{\boldsymbol{\eta}}^M + \begin{bmatrix} 1 & 0 \\ 0 & -1 \end{bmatrix} \hat{\boldsymbol{\zeta}}^M. \tag{70}$$

Performing the necessary operations, we get

$$
\begin{aligned}
W^M(\hat{\boldsymbol{k}}^M, \hat{\boldsymbol{s}}^M, \rho) &= \langle\psi|\hat{\mathsf{P}}|\psi\rangle \\
&= \sum_{I,I_1,I_2} \sum_{\mu_1^M,\mu_2^M} \sum_{\nu_1^M,\nu_2^M} \int d\Theta_{k_1}^M \int d\Theta_{k_2}^M \, c^*_{I_1,\vec{\boldsymbol{k}}_1^M,\mu_1^M} c_{I_2,\vec{\boldsymbol{k}}_2^M,\mu_2^M} \langle I_1\Psi^{(-)}_{I_1,\vec{\boldsymbol{k}}_1^M,\mu_1^M} | I\Psi^{(-)}_{I,\vec{\boldsymbol{k}}^M,\nu_1^M}\rangle \\
&\quad \times \left[\frac{\mathbb{I} + \hat{\boldsymbol{s}}^M \cdot \hat{\boldsymbol{\sigma}}^M}{2}\right]_{\nu_2^M,\nu_1^M} \langle I\Psi^{(-)}_{I,\vec{\boldsymbol{k}}^M,\nu_2^M} | I_2\Psi^{(-)}_{I_2,\vec{\boldsymbol{k}}_2^M,\mu_2^M}\rangle \\
&= \frac{1}{2} \sum_{I,\mu_1,\mu_2} c^*_{I,\vec{\boldsymbol{k}}^M,\mu_1^M} c_{I,\vec{\boldsymbol{k}}^M,\mu_2^M} \left(\delta_{\mu_1^M,\mu_2^M} + \hat{\boldsymbol{s}}^M \cdot \hat{\boldsymbol{\sigma}}^M_{\mu_2^M,\mu_1^M}\right) \\
&= \frac{1}{2} \sum_{I,\mu_1^M,\mu_2^M} \left(\vec{\boldsymbol{D}}^{L*}_{I,\vec{\boldsymbol{k}}^M,\mu_1^M} \cdot \vec{\boldsymbol{E}}^{L*}\right) \left(\vec{\boldsymbol{D}}^{L}_{I,\vec{\boldsymbol{k}}^M,\mu_2^M} \cdot \vec{\boldsymbol{E}}^{L}\right) \left(\delta_{\mu_1^M,\mu_2^M} + \hat{\boldsymbol{s}}^L \cdot \hat{\boldsymbol{\sigma}}^L_{\mu_2^M,\mu_1^M}\right),
\end{aligned}
\tag{71}
$$

which follows from the orthogonality relation

$$
\langle I_1\Psi^{(-)}_{I_1,\vec{\boldsymbol{k}}_1,\mu_1} | I_2\Psi^{(-)}_{I_2\vec{\boldsymbol{k}}_2,\mu_2}\rangle = \delta(\vec{\boldsymbol{k}}_1 - \vec{\boldsymbol{k}}_2)\delta_{\mu_1,\mu_2}\delta_{I_1,I_2}. \tag{72}
$$

We have also introduced vector

$$
\hat{\boldsymbol{\sigma}}^L_{\mu_2^M,\mu_1^M} = \langle\chi_{\mu_2^M}|\hat{\boldsymbol{\sigma}}^L|\chi_{\mu_1^M}\rangle = \langle\chi_{\mu_2^M}|R_\rho\hat{\boldsymbol{\sigma}}^M|\chi_{\mu_1^M}\rangle = R_\rho\hat{\boldsymbol{\sigma}}^M_{\mu_2^M,\mu_1^M} \tag{73}
$$

where R_ρ is rotation matrix,

$$
\hat{\boldsymbol{\sigma}}^M_{\pm\frac{1}{2},\pm\frac{1}{2}} = \pm\hat{\boldsymbol{\zeta}}^M \quad , \quad \hat{\boldsymbol{\sigma}}^M_{\pm\frac{1}{2},\mp\frac{1}{2}} = \hat{\boldsymbol{\xi}}^M \mp i\hat{\boldsymbol{\eta}}^M = \hat{\boldsymbol{\sigma}}^{M*}_{\mp\frac{1}{2},\pm\frac{1}{2}}. \tag{74}
$$

The last line of Eq. (71) also follows from the relation $\hat{\boldsymbol{s}}^L \cdot \hat{\boldsymbol{\sigma}}^L_{\mu_2^M,\mu_1^M} = \hat{\boldsymbol{s}}^M \cdot \hat{\boldsymbol{\sigma}}^M_{\mu_2^M,\mu_1^M}$.

The main results of the paper will involve the average over all molecular orientations of the momentum- and spin-resolved photoionization yield $W^M(\hat{\boldsymbol{k}}^M, \hat{\boldsymbol{s}}^M, \rho)$, Eq. (71), where, the orientation $\rho \equiv \alpha\beta\gamma$ is defined by the Euler angles in the zyz-convention. Now, Eq. (71) fixes the photoelectron momentum and spin-detection axis in the molecular and laboratory frame, respectively, in order to simplify the evaluation of Eq. (71). By doing so, the transition dipole matrix

element in the molecular frame $\vec{\boldsymbol{D}}^{M}_{I,\vec{\boldsymbol{k}}^{M},\mu^{M}}$ will not have any argument that depends on the orientation ρ, and can therefore be trivially rotated into the lab frame:

$$\begin{aligned}\vec{\boldsymbol{D}}^{L}_{I,\vec{\boldsymbol{k}}^{M},\mu^{M}} =&\langle I\Psi^{(-)}_{I,\vec{\boldsymbol{k}}^{M},\mu^{M}}|\vec{\boldsymbol{d}}^{L}|\psi_o\rangle = \langle I\Psi^{(-)}_{I,\vec{\boldsymbol{k}}^{M},\mu^{M}}|R_\rho\vec{\boldsymbol{d}}^{M}|\psi_o\rangle \\ =&R_\rho\langle I\Psi^{(-)}_{I,\vec{\boldsymbol{k}}^{M},\mu^{M}}|\vec{\boldsymbol{d}}^{M}|\psi_o\rangle = R_\rho\vec{\boldsymbol{D}}^{M}_{I,\vec{\boldsymbol{k}}^{M},\mu^{M}}.\end{aligned} \tag{75}$$

Meanwhile, by fixing the spin-detection axis in the lab frame, the spin projection operator $\hat{\mathsf{P}}_{\hat{\boldsymbol{s}}} = \left(\mathbb{I} + \hat{\boldsymbol{s}}^{L}\cdot\hat{\boldsymbol{\sigma}}^{L}\right)/2$ essentially rotates the direction of photoelectron spin from the molecular to the laboratory frame, then projects it to the spin-detection axis $\hat{\boldsymbol{s}}^{L}$:

$$\hat{\boldsymbol{s}}^{L}\cdot\hat{\boldsymbol{\sigma}}^{L}_{\mu_1^{M},\mu_2^{M}} = \hat{\boldsymbol{s}}^{L}\cdot\langle\chi_{\mu_1^{M}}|R_\rho\hat{\boldsymbol{\sigma}}^{M}|\chi_{\mu_2^{M}}\rangle = \hat{\boldsymbol{s}}^{L}\cdot R_\rho\langle\chi_{\mu_1^{M}}|\hat{\boldsymbol{\sigma}}^{M}|\chi_{\mu_2^{M}}\rangle = \hat{\boldsymbol{s}}^{L}\cdot\left(R_\rho\hat{\boldsymbol{\sigma}}^{M}_{\mu_1^{M},\mu_2^{M}}\right). \tag{76}$$

Equation (71) can thus be written as

$$\begin{aligned}&W^{M}(\hat{\boldsymbol{k}}^{M},\hat{\boldsymbol{s}}^{M},\rho) \\ =&\frac{1}{2}\sum_{I,\mu_1^{M},\mu_2^{M}}\left[\left(R_\rho\vec{\boldsymbol{D}}^{M*}_{I,\vec{\boldsymbol{k}}^{M},\mu_1^{M}}\right)\cdot\vec{\boldsymbol{E}}^{L*}\right]\left[\left(R_\rho\vec{\boldsymbol{D}}^{M}_{I,\vec{\boldsymbol{k}}^{M},\mu_2^{M}}\right)\cdot\vec{\boldsymbol{E}}^{L}\right]\left\{\delta_{\mu_1^{M},\mu_2^{M}} + \left[\hat{\boldsymbol{s}}^{L}\cdot\left(R_\rho\hat{\boldsymbol{\sigma}}^{M}_{\mu_2^{M},\mu_1^{M}}\right)\right]\right\}\end{aligned} \tag{77}$$

The vectors that appear on the right-hand side of Eq. (77) can now be grouped into two sets: (i) vectors that are fixed in the molecular frame such as the dipole transition vectors $\vec{\boldsymbol{D}}^{M}_{I,\vec{\boldsymbol{k}}^{M},\mu^{M}}$, photoelectron momentum $\vec{\boldsymbol{k}}^{M}$, and photoelectron spin expectation value $\hat{\boldsymbol{\sigma}}^{M}_{\mu_1^{M},\mu_2^{M}}$, and (ii) vectors that are fixed in the laboratory frame such as spin detection axis $\hat{\boldsymbol{s}}^{L}$ and the electric field $\vec{\boldsymbol{E}}^{L}$. This will then allow us to use the technique in Ref. [42] in evaluating the orientation averaging $\int d\rho$ such that the resulting quantity can be expressed as $\sum_{ij} g_i M_{ij} f_j$, where, g_i and f_i are rotational invariants that are constructed from the two sets of vectors and M_{ij} is the coupling between the

two rotational invariants. For our purposes, the following vector identities will be relevant:

$$\int d\rho(\vec{\boldsymbol{a}}^L \cdot \vec{\boldsymbol{u}}^L)\vec{\boldsymbol{b}}^L = \frac{1}{3}(\vec{\boldsymbol{a}}^M \cdot \vec{\boldsymbol{b}}^M)\vec{\boldsymbol{u}}^L \tag{78}$$

$$\int d\rho(\vec{\boldsymbol{a}}^L \cdot \vec{\boldsymbol{u}}^L)(\vec{\boldsymbol{b}}^L \cdot \vec{\boldsymbol{v}}^L)\vec{\boldsymbol{c}}^L = \frac{1}{6}[(\vec{\boldsymbol{a}}^M \times \vec{\boldsymbol{b}}^M) \cdot \vec{\boldsymbol{c}}^M](\vec{\boldsymbol{u}}^L \times \vec{\boldsymbol{v}}^L) \tag{79}$$

$$\begin{aligned}
&\int d\rho(\vec{\boldsymbol{a}}^L \cdot \vec{\boldsymbol{u}}^L)(\vec{\boldsymbol{b}}^L \cdot \vec{\boldsymbol{v}}^L)(\vec{\boldsymbol{c}}^L \cdot \vec{\boldsymbol{w}}^L)\vec{\boldsymbol{d}}^L \\
&\quad = \frac{1}{30}\begin{bmatrix} (\vec{\boldsymbol{a}}^M \cdot \vec{\boldsymbol{b}}^M)(\vec{\boldsymbol{c}}^M \cdot \vec{\boldsymbol{d}}^M) \\ (\vec{\boldsymbol{a}}^M \cdot \vec{\boldsymbol{c}}^M)(\vec{\boldsymbol{b}}^M \cdot \vec{\boldsymbol{d}}^M) \\ (\vec{\boldsymbol{a}}^M \cdot \vec{\boldsymbol{d}}^M)(\vec{\boldsymbol{b}}^M \cdot \vec{\boldsymbol{c}}^M) \end{bmatrix}^T \begin{bmatrix} 4 & -1 & -1 \\ -1 & 4 & -1 \\ -1 & -1 & 4 \end{bmatrix} \begin{bmatrix} (\vec{\boldsymbol{u}}^L \cdot \vec{\boldsymbol{v}}^L)\vec{\boldsymbol{w}}^L \\ (\vec{\boldsymbol{u}}^L \cdot \vec{\boldsymbol{w}}^L)\vec{\boldsymbol{v}}^L \\ (\vec{\boldsymbol{v}}^L \cdot \vec{\boldsymbol{w}}^L)\vec{\boldsymbol{u}}^L \end{bmatrix}
\end{aligned} \tag{80}$$

Let us now consider the spin-conditioned expectation value of the molecular orientation under isotropic illumination:

$$\left\langle \langle \hat{\boldsymbol{e}}^L \rangle_{\hat{\boldsymbol{s}}^L} \right\rangle_\rho^{\text{iso}} \equiv \frac{\int d\Theta_k^M \int d\Theta_p \int d\rho W^M(\hat{\boldsymbol{k}}^M, \hat{\boldsymbol{s}}^M, \rho)\vec{\boldsymbol{e}}^L}{\int d\Theta_s^L \int d\Theta_k^M \int d\Theta_p \int d\rho W^M(\hat{\boldsymbol{k}}^M, \hat{\boldsymbol{s}}^M, \rho)} \tag{81}$$

Instead of a single direction that characterizes the direction of polarization, e.g., $\hat{\boldsymbol{x}}^L$, we introduce the light field

$$\vec{\boldsymbol{E}}_p^L = E_\omega^L \left(\sin\theta_p \cos\varphi_p \hat{\boldsymbol{x}}^L + \sin\theta_p \sin\varphi_p \hat{\boldsymbol{y}}^L + \cos\theta_p \hat{\boldsymbol{z}}^L\right) \tag{82}$$

Substituting Eq. (77) into the numerator of Eq. (81) we get

$$\begin{aligned}
&\int d\Theta_k^M \int d\Theta_p \int d\rho W^M(\hat{\boldsymbol{k}}^M, \hat{\boldsymbol{s}}^M, \rho)\vec{\boldsymbol{e}}^L \\
&\quad = \frac{1}{2}\sum_{I,\mu_1^M,\mu_2^M} \int d\Theta_k^M \int d\Theta_p \int d\rho \left(\vec{\boldsymbol{D}}^{L*}_{I,\vec{\boldsymbol{k}}^M,\mu_1^M} \cdot \vec{\boldsymbol{E}}_p^{L*}\right)\left(\vec{\boldsymbol{D}}^{L}_{I,\vec{\boldsymbol{k}}^M,\mu_2^M} \cdot \vec{\boldsymbol{E}}_p^{L}\right)
\end{aligned}$$

$$\times \left(\delta_{\mu_1^M,\mu_2^M} + \hat{\boldsymbol{s}}^L \cdot \hat{\boldsymbol{\sigma}}_{\mu_2^M,\mu_1^M}\right) \vec{\boldsymbol{e}}^L \tag{83}$$

Using Eq. (79), the first term of Eq. (83) simplifies into

$$\begin{aligned}
&\frac{1}{2}\sum_{I,\mu}\int d\Theta_k^M \int d\Theta_p \int d\rho \left|\vec{\boldsymbol{D}}^L_{\vec{\boldsymbol{k}}^M,\mu^M} \cdot \vec{\boldsymbol{E}}_p^L\right|^2 \vec{\boldsymbol{e}}^L \\
&\quad = \frac{1}{12}\left\{\left[\sum_{I,\mu}\int d\Theta_k^M \left(\vec{\boldsymbol{D}}^{M*}_{\vec{\boldsymbol{k}}^M,\mu^M} \times \vec{\boldsymbol{D}}^M_{\vec{\boldsymbol{k}}^M,\mu^M}\right)\right]\cdot \vec{\boldsymbol{e}}^M\right\}\left[\int d\Theta_p \left(\vec{\boldsymbol{E}}_p^{L*} \times \vec{\boldsymbol{E}}_p^L\right)\right] = 0,
\end{aligned} \tag{84}$$

which vanishes after averaging over all orientations of the field. Similarly, it follows from Eq. (80) that the second term of Eq. (83)

$$\begin{aligned}
&\frac{1}{2}\sum_{I,\mu_1^M,\mu_2^M}\int d\Theta_k^M \int d\Theta_p \int d\rho \left(\vec{\boldsymbol{D}}^{L*}_{I,\vec{\boldsymbol{k}}^M,\mu_1^M} \cdot \vec{\boldsymbol{E}}_p^{L*}\right)\left(\vec{\boldsymbol{D}}^{L}_{I,\vec{\boldsymbol{k}}^M,\mu_2^M} \cdot \vec{\boldsymbol{E}}_p^{L}\right)\left(\hat{\boldsymbol{s}}^L \cdot \hat{\boldsymbol{\sigma}}^L_{\mu_2^M,\mu_1^M}\right)\vec{\boldsymbol{e}}^L \\
&\quad = \frac{1}{60}\begin{bmatrix}
\sum\int d\Theta_k^M \left(\vec{\boldsymbol{D}}^{M*}_{I,\vec{\boldsymbol{k}}^M,\mu_1^M} \cdot \vec{\boldsymbol{D}}^{M}_{I,\vec{\boldsymbol{k}}^M,\mu_2^M}\right)\left(\hat{\boldsymbol{\sigma}}^M_{\mu_2^M,\mu_1^M} \cdot \vec{\boldsymbol{e}}^M\right) \\
\sum\int d\Theta_k^M \left(\vec{\boldsymbol{D}}^{M*}_{I,\vec{\boldsymbol{k}}^M,\mu_1^M} \cdot \hat{\boldsymbol{\sigma}}^M_{\mu_2^M,\mu_1^M}\right)\left(\vec{\boldsymbol{D}}^{M}_{I,\vec{\boldsymbol{k}}^M,\mu_2^M} \cdot \vec{\boldsymbol{e}}^M\right) \\
\sum\int d\Theta_k^M \left(\vec{\boldsymbol{D}}^{M*}_{I,\vec{\boldsymbol{k}}^M,\mu_1^M} \cdot \vec{\boldsymbol{e}}^M\right)\left(\vec{\boldsymbol{D}}^{M}_{I,\vec{\boldsymbol{k}}^M,\mu_2^M} \cdot \hat{\boldsymbol{\sigma}}^M_{\mu_2^M,\mu_1^M}\right)
\end{bmatrix}^T \\
&\qquad \times \begin{bmatrix} 4 & -1 & -1 \\ -1 & 4 & -1 \\ -1 & -1 & 4 \end{bmatrix}\begin{bmatrix}
\int d\Theta_p |\vec{\boldsymbol{E}}_p^L|^2 \hat{\boldsymbol{s}}^L \\
\int d\Theta_p (\vec{\boldsymbol{E}}_p^{L*} \cdot \hat{\boldsymbol{s}}^L)\vec{\boldsymbol{E}}_p^L \\
\int d\Theta_p (\vec{\boldsymbol{E}}_p^{L} \cdot \hat{\boldsymbol{s}}^L)\vec{\boldsymbol{E}}_p^{L*}
\end{bmatrix} \\
&\quad = \frac{1}{60}\begin{bmatrix} g_1 \\ g_2 \\ g_2^* \end{bmatrix}^T \begin{bmatrix} 4 & -1 & -1 \\ -1 & 4 & -1 \\ -1 & -1 & 4 \end{bmatrix}\begin{bmatrix} f_1 \\ f_2 \\ f_2^* \end{bmatrix} \\
&\quad = \frac{1}{30}\left(2f_1 - \mathrm{Re}[f_2]\right) g_1 - \frac{1}{30}\left(f_1 - 3\mathrm{Re}[f_2]\right)\mathrm{Re}[g_2] - \frac{1}{6}\mathrm{Im}[f_2]\mathrm{Im}[g_2]
\end{aligned} \tag{85}$$

Averaging over all orientations of the field, the second term of Eq. (83) now simplifies into

$$\begin{aligned}
&\frac{1}{2}\sum_{I,\mu_1^M,\mu_2^M}\int d\Theta_k^M\int d\Theta_p\int d\rho\left(\vec{\boldsymbol{D}}^{L*}_{I,\vec{\boldsymbol{k}}^M,\mu_1^M}\cdot\vec{\boldsymbol{E}}_p^{L*}\right)\left(\vec{\boldsymbol{D}}^{L}_{I,\vec{\boldsymbol{k}}^M,\mu_2^M}\cdot\vec{\boldsymbol{E}}_p^{L}\right)\left(\hat{\boldsymbol{s}}^L\cdot\hat{\boldsymbol{\sigma}}^L_{\mu_2^M,\mu_1^M}\right)\vec{\boldsymbol{e}}^L\\
&\quad=\frac{|E_\omega^L|^2}{18}\left\{\left[\sum_{I,\mu_1^M,\mu_2^M}\int d\Theta_k^M\left(\vec{\boldsymbol{D}}^{M*}_{I,\vec{\boldsymbol{k}}^M,\mu_1^M}\cdot\vec{\boldsymbol{D}}^{M}_{I,\vec{\boldsymbol{k}}^M,\mu_2^M}\right)\hat{\boldsymbol{\sigma}}^M_{\mu_2^M,\mu_1^M}\right]\cdot\vec{\boldsymbol{e}}^M\right\}\hat{\boldsymbol{s}}^L\\
&\quad=\frac{|E_\omega^L|^2S_0}{18}(\vec{\boldsymbol{S}}^M\cdot\vec{\boldsymbol{e}}^M)\hat{\boldsymbol{s}}^L.
\end{aligned}\tag{86}$$

Last, the denominator of Eq. (81) simplifies into

$$\begin{aligned}
&\int d\Theta_s^L\int d\Theta_k^M\int d\Theta_p\int d\rho W^M(\hat{\boldsymbol{k}}^M,\hat{\boldsymbol{s}}^M,\rho)\\
&\quad=\frac{|E_\omega^L|^2}{6}\sum_{I,\mu}\int d\Theta_k^M\left|\vec{\boldsymbol{D}}^M_{I,\vec{\boldsymbol{k}}^M,\mu_2^M}\right|^2=\frac{|E_\omega^L|^2}{6}S_0
\end{aligned}\tag{87}$$

Thus, we finally obtain

$$\left\langle\langle\hat{\boldsymbol{e}}^L\rangle_{\hat{\boldsymbol{s}}^L}\right\rangle_\rho^{\text{iso}}=\frac{1}{3}(\vec{\boldsymbol{S}}^M\cdot\vec{\boldsymbol{e}}^M)\hat{\boldsymbol{s}}^L\tag{88}$$

A similar straightforward calculation for a light field polarized along $\hat{\boldsymbol{\epsilon}}^L$ will yield

$$\left\langle\langle\hat{\boldsymbol{e}}^L\rangle_{\hat{\boldsymbol{s}}^L}\right\rangle_\rho=\frac{1}{5}\left[\left(2\vec{\boldsymbol{S}}^M+\vec{\boldsymbol{S}}'^M\right)\right]\hat{\boldsymbol{s}}^L-\frac{1}{5}\left[\left(\vec{\boldsymbol{S}}^M+3\vec{\boldsymbol{S}}'^M\right)\right](\hat{\boldsymbol{s}}^L\cdot\hat{\boldsymbol{\epsilon}}^L)\hat{\boldsymbol{\epsilon}}^L.\tag{89}$$

1. Evers, F. *et al.* Theory of chirality induced spin selectivity: Progress and challenges. *Advanced Materials* **34**, 2106629 (2022).

2. Aiello, C. D. *et al.* A chirality-based quantum leap. *ACS nano* **16**, 4989–5035 (2022).

3. Gaita-Ariño, A., Luis, F., Hill, S. & Coronado, E. Molecular spins for quantum computation. *Nature chemistry* **11**, 301–309 (2019).

4. Atzori, M. & Sessoli, R. The second quantum revolution: role and challenges of molecular chemistry. *Journal of the American Chemical Society* **141**, 11339–11352 (2019).

5. Wasielewski, M. R. *et al.* Exploiting chemistry and molecular systems for quantum information science. *Nature Reviews Chemistry* **4**, 490–504 (2020).

6. Carretta, S., Zueco, D., Chiesa, A., Gómez-León, Á. & Luis, F. A perspective on scaling up quantum computation with molecular spins. *Applied Physics Letters* **118** (2021).

7. Heinrich, A. J. *et al.* Quantum-coherent nanoscience. *Nature nanotechnology* **16**, 1318–1329 (2021).

8. Chiesa, A. *et al.* Chirality-induced spin selectivity: An enabling technology for quantum applications. *Advanced Materials* **35**, 2300472 (2023).

9. Ray, K., Ananthavel, S., Waldeck, D. & Naaman, R. Asymmetric scattering of polarized electrons by organized organic films of chiral molecules. *Science* **283**, 814–816 (1999).

10. Ray, S., Daube, S., Leitus, G., Vager, Z. & Naaman, R. Chirality-induced spin-selective properties of self-assembled monolayers of dna on gold. *Physical review letters* **96**, 036101 (2006).

11. Muhlbauer, S. *et al.* Skyrmion lattice in a chiral magnet. *Science* **323**, 915–919 (2009).

12. Nagaosa, N. & Tokura, Y. Topological properties and dynamics of magnetic skyrmions. *Nature nanotechnology* **8**, 899–911 (2013).

13. Kettner, M. *et al.* Chirality-dependent electron spin filtering by molecular monolayers of helicenes. *The journal of physical chemistry letters* **9**, 2025–2030 (2018).

14. Mishra, D. *et al.* Spin-dependent electron transmission through bacteriorhodopsin embedded in purple membrane. *Proceedings of the National Academy of Sciences* **110**, 14872–14876 (2013).

15. Kettner, M., Bhowmick, D. K., Bartsch, M., Göhler, B. & Zacharias, H. A silicon-based room temperature spin source without magnetic layers. *Advanced Materials Interfaces* **3** (2016).

16. Yeganeh, S., Ratner, M. A., Medina, E. & Mujica, V. Chiral electron transport: Scattering through helical potentials. *The Journal of chemical physics* **131** (2009).

17. Medina, E., López, F., Ratner, M. A. & Mujica, V. Chiral molecular films as electron polarizers and polarization modulators. *Europhysics Letters* **99**, 17006 (2012).

18. Eremko, A. & Loktev, V. Spin sensitive electron transmission through helical potentials. *Physical Review B—Condensed Matter and Materials Physics* **88**, 165409 (2013).

19. Varela, S., Medina, E., Lopez, F. & Mujica, V. Inelastic electron scattering from a helical potential: transverse polarization and the structure factor in the single scattering approximation. *Journal of Physics: Condensed Matter* **26**, 015008 (2013).

20. Gutierrez, R., Díaz, E., Naaman, R. & Cuniberti, G. Spin-selective transport through helical molecular systems. *Physical Review B—Condensed Matter and Materials Physics* **85**, 081404 (2012).

21. Guo, A.-M. & Sun, Q.-f. Spin-selective transport of electrons in dna double helix. *Physical review letters* **108**, 218102 (2012).

22. Matityahu, S., Utsumi, Y., Aharony, A., Entin-Wohlman, O. & Balseiro, C. A. Spin-dependent transport through a chiral molecule in the presence of spin-orbit interaction and nonunitary effects. *Physical Review B* **93**, 075407 (2016).

23. Varela, S., Mujica, V. & Medina, E. Effective spin-orbit couplings in an analytical tight-binding model of dna: Spin filtering and chiral spin transport. *Physical Review B* **93**, 155436 (2016).

24. Peter, J. S., Ostermann, S. & Yelin, S. F. Chirality dependent photon transport and helical superradiance. *Phys. Rev. Res.* **6**, 023200 (2024). URL https://link.aps.org/doi/10.1103/PhysRevResearch.6.023200.

25. Maslyuk, V. V., Gutierrez, R., Dianat, A., Mujica, V. & Cuniberti, G. Enhanced magnetoresistance in chiral molecular junctions. *The journal of physical chemistry letters* **9**, 5453–5459 (2018).

26. Díaz, E., Domínguez-Adame, F., Gutierrez, R., Cuniberti, G. & Mujica, V. Thermal decoherence and disorder effects on chiral-induced spin selectivity. *The journal of physical chemistry letters* **9**, 5753–5758 (2018).

27. Zoöllner, M. S., Varela, S., Medina, E., Mujica, V. & Herrmann, C. Insight into the origin of chiral-induced spin selectivity from a symmetry analysis of electronic transmission. *Journal of chemical theory and computation* **16**, 2914–2929 (2020).

28. Ghazaryan, A., Lemeshko, M. & Volosniev, A. G. Filtering spins by scattering from a lattice of point magnets. *Communications Physics* **3**, 178 (2020).

29. Fransson, J. Chirality-induced spin selectivity: The role of electron correlations. *The journal of physical chemistry letters* **10**, 7126–7132 (2019).

30. Fransson, J. Vibrational origin of exchange splitting and" chiral-induced spin selectivity. *Physical Review B* **102**, 235416 (2020).

31. Vittmann, C., Lim, J., Tamascelli, D., Huelga, S. F. & Plenio, M. B. Spin-dependent momentum conservation of electron–phonon scattering in chirality-induced spin selectivity. *The Journal of Physical Chemistry Letters* **14**, 340–346 (2023).

32. Bian, X. *et al.* Modeling nonadiabatic dynamics with degenerate electronic states, intersystem crossing, and spin separation: A key goal for chemical physics. *The Journal of Chemical Physics* **154** (2021).

33. Teh, H.-H., Dou, W. & Subotnik, J. E. Spin polarization through a molecular junction based on nuclear berry curvature effects. *Physical Review B* **106**, 184302 (2022).

34. Shitade, A. & Minamitani, E. Geometric spin–orbit coupling and chirality-induced spin selectivity. *New Journal of Physics* **22**, 113023 (2020).

35. Ordonez, A. F. & Smirnova, O. Propensity rules in photoelectron circular dichroism in chiral molecules. i. chiral hydrogen. *Physical Review A* **99**, 043416 (2019).

36. Samson, J. & Stolte, W. Precision measurements of the total photoionization cross-sections of He, Ne, Ar, Kr, and Xe. *Journal of Electron Spectroscopy and Related Phenomena* **123**, 265–276 (2002). URL http://dx.doi.org/10.1016/S0368-2048(02)00026-9.

37. Carlström, S. *et al.* Spin-polarized photoelectrons in the vicinity of spectral features. *Physical Review Letters* **134**, 093202 (2025).

38. Campbell, D. & Farago, P. Electron optic dichroism in camphor. *Journal of Physics B: Atomic and Molecular Physics* **20**, 5133 (1987).

39. Mayer, S. & Kessler, J. Experimental verification of electron optic dichroism. *Physical review letters* **74**, 4803 (1995).

40. Carlström, S., Spanner, M. & Patchkovskii, S. General time-dependent configuration-interaction singles. i. molecular case. *Physical Review A* **106**, 043104 (2022).

41. Carlström, S., Bertolino, M., Dahlström, J. M. & Patchkovskii, S. General time-dependent configuration-interaction singles. ii. atomic case. *Physical Review A* **106**, 042806 (2022).

42. Andrews, D. L. & Thirunamachandran, T. On three-dimensional rotational averages. *The Journal of Chemical Physics* **67**, 5026–5033 (1977).

43. Ordonez, A. F., Ayuso, D., Decleva, P. & Smirnova, O. Geometric magnetism and anomalous enantio-sensitive observables in photoionization of chiral molecules. *Communications Physics* **6**, 257 (2023).

44. Nicklass, A., Dolg, M., Stoll, H. & Preuss, H. *Ab Initio* energy-adjusted pseudopotentials for the noble gases Ne through Xe: Calculation of atomic dipole and quadrupole polarizabilities. *The Journal of Chemical Physics* **102**, 8942–8952 (1995). URL https://doi.org/10.1063/1.468948.

45. Pabst, S., Lein, M. & Wörner, H. J. Preparing attosecond coherences by strong-field ionization. *Physical Review A* **93**, 023412 (2016). URL http://dx.doi.org/10.1103/PhysRevA.93.023412.

46. Zapata, F., Vinbladh, J., Ljungdahl, A., Lindroth, E. & Dahlström, J. M. Relativistic time-dependent configuration-interaction singles method. *Physical Review A* **105**, 012802 (2022). URL http://dx.doi.org/10.1103/PhysRevA.105.012802.

47. Ruberti, M., Averbukh, V. & Mintert, F. Bell test of quantum entanglement in attosecond photoionization. *Physical Review X* **14**, 041042 (2024). URL http://dx.doi.org/10.1103/PhysRevX.14.041042.

48. Mogensen, P. K. & Riseth, A. N. Optim: A mathematical optimization package for Julia. *Journal of Open Source Software* **3**, 615 (2018).